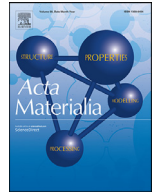




ELSEVIER

Contents lists available at ScienceDirect

Acta Materialia

journal homepage: www.elsevier.com/locate/actamat

Modelling of additive manufacturability of nickel-based superalloys for laser powder bed fusion

Jinghao Xu^a, Paraskevas Kontis^{b,c}, Ru Lin Peng^a, Johan Moverare^{a,*}

^a Division of Engineering Materials, Linköping University, Linköping SE-58183, Sweden

^b Max-Planck-Institut für Eisenforschung, Max-Planck Straße 1, Düsseldorf 40237, Germany

^c Department of Materials Science and Engineering, NTNU Norwegian University of Science and Technology, Trondheim 7491, Norway

ARTICLE INFO

Article history:

Received 8 August 2021

Revised 26 August 2022

Accepted 26 August 2022

Available online 29 August 2022

Keywords:

Laser powder bed fusion (LPBF)

Cracking susceptibility

Micro-segregation

Alloy compositions

Printability

ABSTRACT

The additive manufacturability of nickel-based superalloys for laser powder bed fusion (LPBF) technologies is studied by considering the in-process cracking mechanisms. The additive manufacturability of nickel-based superalloys largely depends on the resistance to the liquid and solid-state cracking. Herein, we propose a two-parameter-based, heat resistance and deformation resistance (HR-DR) model, accounting for the relation between chemical composition (both major and minor elements) and cracking susceptibility, which is generalized from the elemental microsegregation behavior and mechanisms of LPBF process induced cracking. The proposed model is validated by the LPBF experiments in this study and by the hitherto reported data in LPBF superalloys community. The HR-DR-model is found to be a theoretically acceptable and easy-to-use approach for the prediction of in-process cracking of nickel-based superalloys during LPBF. The influence of alloying elements and the γ' precipitates on the additive manufacturability is discussed. The model provides a path for designing not only new solid solutioning, but also and more importantly γ' strengthened nickel-based superalloys for LPBF applications.

© 2022 The Author(s). Published by Elsevier Ltd on behalf of Acta Materialia Inc.

This is an open access article under the CC BY license (<http://creativecommons.org/licenses/by/4.0/>)

1. Introduction

Laser powder bed fusion (LPBF) is a rapidly developing additive manufacturing (AM) technique. It uses a laser as the high energy-density source to locally fuse the material within a powder bed continuously, resulting in the successive layer-by-layer building in a three-dimensional manner. Considering the melting and solidification procedures locally, LPBF shows obvious similarity to a welding process [1]. To this sense, the alloys included into the materials portfolio are from the 'weldable' category. This limitation undoubtedly precludes a large group of advanced alloys, such as the precipitation-strengthened nickel-based superalloys with relatively high contents of Al and Ti, from the implementation of the LPBF process, owing to their 'non-weldable' nature [2].

Nickel-based superalloys are the alloy system based on nickel as the matrix element with up to 10 or more alloying elements doped [3], and primarily used for components within the hot-section of aeroengine turbines for aviation and industrial gas turbine for power generation [4]. Over the years, the high-temperature mechanical properties and oxidation resistance of nickel-based su-

peralloys have been improved dramatically. The excellent high-temperature mechanical properties of nickel-based superalloys are mainly attributed to the formation of the γ' precipitation-strengthening phase, but also to the contribution by solid-solution strengthening. The γ' phase is an intermetallic phase with a $L1_2$ crystal structure, and the general chemical composition formula is $(\text{Ni, Co})_3(\text{Al, Ti, Ta})$. In fully heat-treated conditions, the desired γ' volume fraction is typically 50–60% [5] in advanced powder metallurgy superalloys for turbine disc applications, and 60–80% [6] in single-crystal superalloys for turbine blade applications. However, with high volume fraction of γ' , the nickel-based superalloys are treated as 'non-weldable' owing to its intrinsic cracking susceptibility. Therefore, the LPBF fabrication of these superalloys is a huge challenge.

Another important contribution to high-temperature mechanical properties derives from the grain boundary (GB) strengthening, by adding minor elements like C and B. The addition of these minor elements is inevitably desired for polycrystalline superalloys from the high-temperature performance perspective. With the addition of C, the desired grain-boundary carbides are formed, which are beneficial to the grain boundary sliding resistance at high temperatures [7]. And with the addition of B, the creep performance is dramatically improved [8]. Kontis et al. [9] reported that in a cast

* Corresponding author.

E-mail address: johan.moverare@liu.se (J. Moverare).

superalloy with 0.05 at.% B, the creep rupture life is more than one order of magnitude longer than for the B-free counterpart.

To this end, the challenge of γ' strengthened superalloy produced by LPBF is attributed to both high γ' fraction and addition of minor elements. High cracking susceptibility of γ' strengthened superalloys is generally found in casting, welding, as well as additive manufacturing. The detailed cracking mechanisms are reviewed in the background section. Facing the issues raised from the high cracking susceptibility of γ' strengthened nickel-based superalloys, it has apparently hindered this critical group of alloys to be robustly adapted for additive manufacturing. A lot of questions could be raised, for example, whether γ' strengthened nickel-based superalloys are totally unprintable, or whether minor elements are still required for printing these alloys to achieve a good print quality, or what is the guideline for the addition of alloying (both major and minor) elements. The key to answering these questions would be a reliable model to predict the additive manufacturability of superalloys.

In this study, the high- γ' -volume-fraction superalloy MAD542, and the intermediate- γ' -volume-fraction superalloy ME3 are investigated with a focus on their printability via various printing parameters. The cracking mechanisms, as-built microstructures, elemental segregation, and suppression of γ' are systematically characterized for the MAD542 superalloy. The cracking mechanisms influencing the additive manufacturability of nickel-based superalloys by LPBF are considered. Based on these mechanisms, a heat resistance and deformation resistance based (HR-DR) model has been proposed to evaluate the LPBF printability of nickel-based superalloys. The chemical composition effects on the printability of superalloys are pin pointed and quantified. In the later section of this paper, the HR-DR model is used to create a generalized additive manufacturability diagram which shows very good agreement with the experimental results in this study as well as data from the literature. Thus, the novel approach to predict LPBF printability of nickel-based superalloys that is proposed in this study captures the critical boundary for printability and shows huge potential to be adapted for alloy design of superalloys for the LPBF process. Potentially, the modelling framework could also be adapted for other alloy systems.

2. Background

Since the major concern in this study is the additive manufacturability with respect to cracking of nickel-based superalloys for LPBF, the fundamental mechanisms that govern the crack formation need to be understood and are therefore briefly reviewed in the following sections. The four generally accepted critical cracking mechanisms related to the LPBF process are summarized below:

2.1. Solidification cracking

For fusion of powders to bulk materials, solidification is an important process. Solidification cracking, also known as hot tearing or hot cracking, happens at the last-stage of the solidification process [10]. Solidification cracking is commonly accepted to occur at the partly solid state and cause irreversible cracks [11,12]. This process can be described as owing to the lack of compensation by liquid flow, the partly solid material is torn apart under the thermal stresses induced by solidification shrinkage [13]. Above the solidus temperature, more precisely above the solidus temperature of the interdendritic microconstituent, cavities and pores are prone to form in this semisolid zone [14] and the cracks could initiate at these sites. While the liquid phase barely sustains the thermal stresses, larger cracks are formed by the crack propagation.

The semisolid zone is critical for solidification cracking susceptibility. By understanding this, several models have been proposed to formulate the solidification cracking susceptibility. The most commonly considered aspect is the solidification range, or freezing range [15]. It is defined as the temperature span of the solidification process, i.e. the range between the liquidus and solidus temperatures [16]. A narrow solidification range provides a narrow semisolid mush. Based on this, a smaller solidification range helps the alloy go through the high cracking susceptibility microstructure quickly in terms of temperature. As reported by Shankar et al. [17], the hot cracking density of a stainless steel reduced from 1.1 to 0.1 mm/mm² by decreasing the solidification range from 68 to 21°C. Other models consider a modified critical solidification range by taking liquid feeding (0–90% solid), and liquid films/droplets transformation (0–94% solid) into account [10]. Similar models could be summarized as replacing the solidification temperature range with solidification time. As proposed by Clyne and Davis [18], the hot cracking sensitivity is assessed by the time interval spent by the mushy zone from liquid to solidus. To step further, the deformation rate index was developed by Rappaz et al. [19] to consider the tensile deformation applied to the normal direction of dendrite growth and solidification time.

Based on these models, the key to reduce solidification cracking susceptibility is to generally reduce the solidification range by increasing the solidus temperature. In the last-stage of solidification, minor elements such as B and Zr tend to segregate to the intergranular boundaries [9], lowering the interface energy of the solid and liquid phases [20]. The deleterious effect of these minor elements on the solidification cracking resistance can be supported by experimental results, as reported by Grodzki et al. [21], where the solidification cracking resistance is improved by decreasing the Zr content from 0.09 wt.% to 0 in a nickel-based superalloy.

2.2. Liquation cracking

Liquation cracking is another commonly observed cracking mechanism in nickel-based superalloys. As the name is referring to, liquation cracking involves the presence of a liquid phase. After the solidification, some localized regions in the solid will be partially liquified by the reheating from the adjacent areas and/or the following added layers. For this reason, in a welding process, the liquation cracking is observed close but away from the melt pool [22].

In welding of γ' strengthened superalloys, the γ/γ' eutectic phase is generally found in the solidification interdendritic region. The solidus temperature of a eutectic phase is lower than the global solidus temperature of the alloy. At a temperature even lower than the overall solidus temperature, the γ/γ' eutectic may be liquified. The microstructure evidence is found from the re-solidified γ/γ' eutectic in the liquation cracking region in the heat affect zone in welding [23]. However, in the additively manufactured γ' superalloys, the γ/γ' eutectic phase is barely observed. In the as-built condition, the microstructure is closer to a super-saturated solid solution. Tang et al. [24] conducted synchrotron X-ray diffraction measurements on a γ' forming nickel-based superalloy from a high energy beamline. In their study, the γ' intensity peaks are absent in the as-built sample while present in the heat-treated sample where γ' has been developed. Under this premise, the liquified γ/γ' eutectic phase is apparently not the causality of liquation cracking in AM.

Another possible mechanism for liquation cracking in AM superalloys is the 'segregation induced liquation' [22]. Reported by Kontis et al. [25], atom probe tomography results proved the severe segregation of minor elements, e.g. boron, to the interdendritic region of an electron beam powder bed fused nickel-based superalloy. The significant enrichment of solutes at the interdendritic

dritic region progressively decreases the localized solidus temperature, which will promote liquation cracking.

Both solidification and liquation cracking could be defined as 'hot' cracking, referring to these types of cracking mechanisms where intergranular liquid films are involved, according to DuPont et al. in their welding textbook [26]. However, after solidification, i.e., in the solid state, cracking could still happen, like strain-age cracking and ductility-dip cracking.

2.3. Strain-age cracking

Strain-age cracking is an unneglectable topic of γ' strengthened nickel-based superalloys, since it is largely associated with the development of γ' precipitates by either aging effects from subsequent layer building and/or the post-processing thermal treatment. In a LPBF as-built sample, large un-relaxed residual stresses are typically left behind [27]. At the aging/stress-relief temperature, two phenomena occur simultaneously, the residual stress relaxation, and the developing of γ' precipitates. Owing to the rapid precipitation kinetic of the γ' phase, the residual stress relaxation is slower than the promotion of γ' [28]. With the increasing of γ' , the ductility is reduced [29]. The remaining residual stress is superposed with the γ' formation induced stress [30] which results in the strain-age cracking.

The strain-age cracking is a critical cracking problem during post-process treatments for γ' strengthened nickel-based superalloys. However, strain-age cracking is less likely to occur in another common class of superalloys, the γ'' strengthened nickel-based superalloys, e.g., IN718 and IN625. The reason is the sluggish γ'' precipitation kinetics [31] resulting in a larger residual stress relaxation window.

2.4. Ductility-dip cracking

The loss in ductility of γ' strengthened nickel-based superalloys is commonly found over a critical intermediate temperature range below solidus. Kim et al. [32] reported the tensile elongation of wrought CM247LC superalloy dramatically reduced between 700–900°C. Németh et al. [33] reported a tensile ductility dip with a valley value less than 4% for the wrought superalloy 720Li. In another superalloy, Monel K-500, the ductility is largely decreased from 20% elongation at 300°C to 2% at 650°C as reported by Young et al. [34]. The ductility-dip cracking typically has intergranular cracking characteristics [35] and it should be stressed that, ductility-dip cracking is sub-solidus cracking occurring in the solid state as defined by Hemsworth et al. [36]. When a superalloy is subjected to the global tensile stresses generated during fusion at the critical ductility-dip temperature range, the ductility-dip cracking could take place [37].

One of the accepted mechanisms for ductility-dip cracking is the inoperability of grain boundary sliding at intermediate temperature, as proposed in [38–40]. On one hand, a lower grain boundary sliding rate has a beneficial effect on creep resistance. The intergranular precipitates, like GB γ' and carbides, are the operative GB pinning source to oppose the GB sliding [41]. The GB morphology also plays an important role, for example, a tortuous GB effectively retarding the GB sliding. On the other hand, the strongly re-

duced ability for GB sliding results in strain concentrations which promotes void initiation. Tang et al. [42] showed that extended accumulation of dislocations is observed on the tortuous GBs as compared to flat GBs, during creep of a superalloy. These dislocation pile-ups along GBs assisted in the void nucleation. Then the growth and linking of these voids formed will lead to ductility-dip cracking.

3. Analysis of selected LPBF superalloys

3.1. Materials and methods

Two nickel-based superalloys, the MAD542 and ME3 alloy were selected as the representative materials in this study. MAD542 [43] is a newly developed nickel-based superalloy adapted for the LPBF process, and ME3 [44] (also known as René 104) is a powder metallurgy nickel-based superalloy designed for turbine engine disk application. Both MAD542 and ME3 are γ' strengthened nickel-based superalloys, where the equilibrium volume fraction of γ' phase is 61% and 53%, respectively, according to thermodynamic calculations at 800°C (ThermoCalc®, TCNI10 database). The pre-alloyed powders for the LPBF process were supplied by Höganäs AB, Sweden. The 15–45 μm sized powders were produced by gas atomization. The chemical composition of the MAD542 and ME3 powders are listed in Table 1. An EOS M100 system equipped with an ytterbium fiber laser source with the power capacity of 200 W was used to fabricate $10 \times 10 \times 10 \text{ mm}^3$ cubic samples. The scanning strategy was chosen to be 67° Rot-scan, indicating the scanning vector rotates 67° between each adjacent layer. To explore the LPBF processing window of these superalloys, 9 sets of printing parameters were applied, as listed in Table 2. The volume energy density, E_v (J/mm^3) was calculated as $E_v = P$ (laser power, W) / V (scan speed, mm/s) / H (hatching distance, mm) / L (layer thickness, mm). All the prints were conducted under an argon atmosphere.

For metallographic sample preparation, a Struers Tegramin system was used with a final polishing in OP-U colloidal silica suspension. In order to form the γ' precipitates in MAD542 superalloy, post-processing heat treatment (1230°C/2h followed by two-step aging: 1080°C/4h and 900°C/24h) was applied using a RO-HDE chamber furnace. Electro-etching at 10 V in a 10% phosphoric acid solution was conducted to reveal the γ' morphology by dissolving the γ matrix. The microstructural characterizations were carried out by a Leica DM6 Optical Microscopy (OM), and a Hitachi SU-70 Scanning Electron Microscopy (SEM) system equipped with an Oxford instrument Electron Backscatter Diffraction (EBSD) detector. The EBSD indexing rates were greater than 93% and 97% for large-scale (step size 1 μm) and small-scale (0.04 μm) scans, respectively. EBSD measurement data was analyzed and visualized using an open-source MATLAB package MTEX [45].

Site specific lift-outs for atom probe tomography (APT) were prepared following the procedures described in Thompson et al. [46] from interdendritic regions of the MAD542 alloy. A FEI Helios Nanolab 600i dual SEM/focused ion beam (FIB) was used for the preparation of the APT specimens. The specimens were analyzed in a Cameca 5000XR instrument, operated at 55 K in laser pulsing mode with laser energy at 50 pJ and a repetition rate of 125

Table 1

The chemical composition of the powders of MAD542 and ME3 nickel-based superalloy investigated in this study.

Alloy	Cr	Co	Mo	W	Al	Ti	Ta	Nb	C	B	Si	Zr	Ni
MAD542 (wt.%)	8.0	8.0	5.0	4.0	5.0	1.0	3.0	2.0	0.1	<0.001	<0.005	<0.002	Bal.
MAD542 (at.%)	9.0	8.0	3.1	1.3	10.9	1.2	1.0	1.3	0.5	<0.005	<0.01	<0.001	Bal.
ME3 (wt.%)	13.1	18.6	3.9	1.7	3.7	3.5	2.5	1.4	0.1	<0.001	0.012	<0.002	Bal.
ME3 (at.%)	14.4	18.2	2.3	0.5	7.9	4.2	0.8	0.9	0.5	<0.005	0.024	<0.001	Bal.

Table 2
Laser powder bed fusion processing parameters used in this study (layer thickness: 20 μm).

Exp.	Laser power, P (W)	Scan speed, V (mm/s)	Hatching distance, H (μm)	Energy density, E_v (J/mm^3)
#1	100	1000	50	100
#2	170	1000	50	170
#3	100	1300	50	77
#4	170	1300	50	131
#5	100	1000	70	71
#6	170	1000	70	121
#7	100	1300	70	55
#8	170	1300	70	93
#9	135	1150	60	98

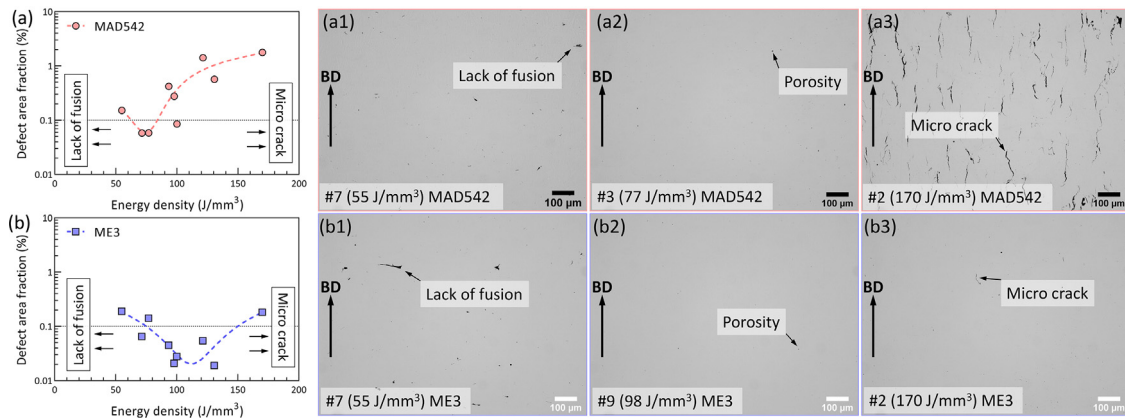


Fig. 1. Plots of defect area fraction as a function of energy density for (a) MAD542 and (b) ME3 superalloys. Optical micrographs of representative as-built MAD542 and ME3 samples indicating three typical LPBF defects: lack of fusion ((a1) MAD542, (b1) ME3), gas porosity ((a2) MAD542, (b2) ME3), and micro-cracks ((a3) MAD542, (b3) ME3).

kHz. Data reconstruction and processing was performed using the Cameca IVAS 3.8.8 software tool.

3.2. Defect density versus process parameters

Fig. 1(a) and (b) shows the summary of the plots of LPBF defect level in the form of area fraction, as a function of energy density for the MAD542 and ME3 superalloys in the as-built condition, respectively. The results are obtained by the combination with metallographic observation of the well-polished and post image analysis.

There are mainly three types of defects observed (Fig. 1(a1–3) for MAD542 and 1(b1–3) for ME3), lack of fusion, gas porosity and micro-cracks. To the lower energy density side, the input energy is insufficient to fuse the powder layer, resulting in these lack of fusion defects. Typically, the longer length of lack of fusion is parallel to the powder bed plane, i.e., normal to the building direction. However, to the higher energy density side, the commonly observed defects are micro-cracks. The mechanisms for these in-process induced cracks are complicated and highly influenced by not only processing parameters (e.g., #7 set of parameters induce lack of fusion mainly, while #2 set of parameters induce micro cracks), but also chemical composition. By applying the same #2 printing parameters in an identical printing system, the cracking susceptibility between the MAD542 and ME3 alloy is obviously different. Another type of common LPBF defect is porosity. It is accepted that the entrapped inert gases aggregate in the solid metal and left as the spherical gas porosity [47].

The optimization of the printing parameters can result in fabricated samples, for both MAD542 and ME3 alloys, in a crack-free condition (Fig. 1(a2) and (b2)). For example, the printing parameters give the valley of the defect fraction as a function of energy density curves. It should be noted that, the gas porosity is still observed in the crack-free sample with a minimum amount. Apparently, according to the optical micrographs as well as the sum-

marized plots, ME3 superalloy has a larger crack-free processing window than MAD542.

3.3. Observed cracking mechanisms

The general cracking modes in LPBF nickel-based superalloys are investigated using the MAD542 sample fabricated by the #4 printing parameters, which has a high energy density for this alloy to induce different types of cracks. Detailed characteristics of the cracks are observed in the SEM-SE micrographs in Fig. 2. Generally, the cracks are closely parallel to the building direction (BD) (Fig. 2(a)). Fig. 2(b, b1) presents the representative feature of hot-tearing cracks. This type of crack is formed at the last stage of solidification before the solid phase is fully developed. The tensile stresses normal to the cracking direction tear the remained liquid phase apart. As in Fig. 2(b1), the solidification dendrite arms are commonly found in the crack cleavage, which is known as reliable evidence of solidification cracking [48,49]. The width of the hot-tearing cracks is in the length scale of several micron-meters.

After solidification, the solid part would be influenced by the intrinsic heating effect from the laser fusion of the adjacent layer (upper layer). If the heating temperature exceeds the solidus temperature of the solid, localized liquification occurs. Generally, the interdendritic region shows a lower solidus temperature than the dendrite core. These localized liquation region results in cracking with the assistance of tensile stress. The length dimension of the width of these cracks are in the sub-micron scale (see Fig. 2(d1)). The remelted liquid film feature is shown in the channel of this type of crack, as in Fig. 2(d1). In the solid part and further away from heating source, e.g., Fig. 2(d2) region in Fig. 2(d), sharp crack tips are observed. In this colder region in Fig. 2(d2) (comparing with Fig. 2(d1)), it may not be liquified. The crack could propagate from the upper liquified region (Fig. 2(d1)) into the lower solid region (Fig. 2(d2)), leading to the decreasing of the crack width. It

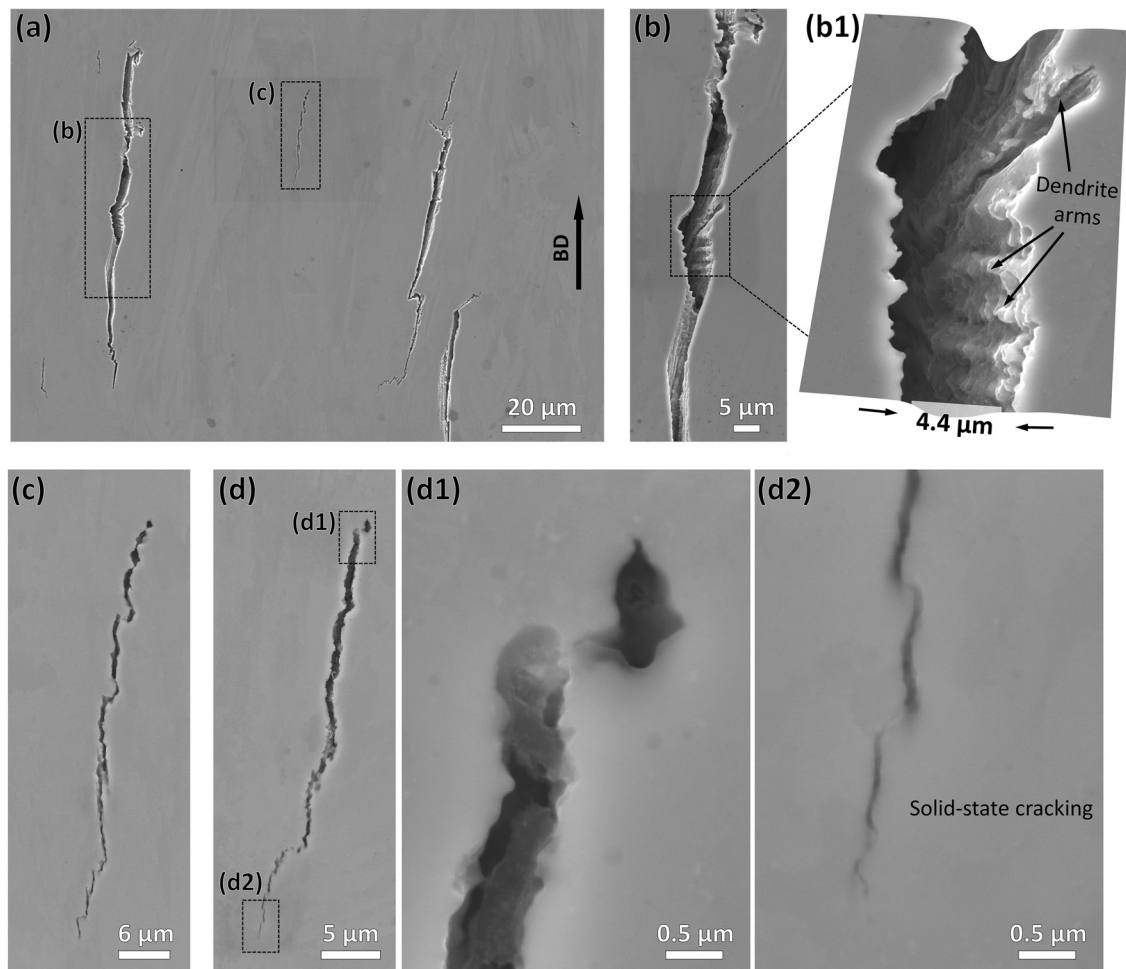


Fig. 2. Different types of micro cracks observed in as-LPBF-processed MAD542 superalloy using #4 printing parameters from SEM-SE imaging, (a) overall viewing of micro-cracks (b) enlarged view of a hot-tearing type crack, (b1) stereo micrograph indicates the dendrite arm features in the hot-tearing crack cleavage, (c, d) mixed type cracks, (d1) enlarged viewing of liquid-state cracking feature at the starting region of the micro-crack shown in (d), and (d2) enlarged viewing of solid-state cracking feature at the ending region. (The building direction is from bottom to top for all the micrographs).

should be mentioned that, at the crack tip (Fig. 2(d2)), the length dimension of solid-state crack is in the nanometer scale.

3.4. Grain boundaries

Fig. 3 shows the EBSD scanning results in the cracked region. In Fig. 3(a), EBSD-band contrast (BC) map illustrates the micro-cracks in darker contrast owing to the lack of indexing. The EBSD-inverse pole figure (IPF) coloring map in Fig. 3(b) shows the columnar grain structure in the as-built microstructure. The (100) pole figure generated by the orientation distribution function (ODF) calculation from the EBSD scanning area is provided in the inset. The columnar grain growth direction is along the BD, resulting in a strong (100) intensity (maximum multiples of uniform density (MUD) = 8) towards the BD. Similar to findings of micro-cracks in the SEM micrographs, the cracks are closely parallel to the BD, i.e., close to the columnar grain direction. SEM-BSE micrographs is presented to reveal the solidification dendrites in an area close to a micro-crack, in Fig. 3(b). In Fig. 3(d), the EBSD-BC map is superposed with the grain boundary (GB) and subgrain boundary plots on the same area of Fig. 3(c). The grain and subgrain boundaries are plotted according to the misorientation angles. The misorientation angle is between 2–15° for subgrain boundaries and >15° for grain boundaries. By combining both Fig. 3(c) and (d), unique features of LPBF microstructure are illustrated. According to the

welding literature [26], the subgrain boundary separating a cluster of cellular dendrites is known as solidification sub-grain boundary (SSGB), while the intersection of SSGBs may lead to a boundary with high angular misorientation known as solidification grain boundaries (SGBs). These GB interfaces were formed at the last stage of the solidification process. In addition, the cracked GBs are misorientation-dependent. As documented by Hariharan et al. [48], cracks are occurring along the high-angle GBs with misorientation angles greater than 15°, but in contrast no crack was found at the low-angle GBs in a LPBF IN738LC superalloy. It is consistent with the observation in Fig. 3, that the crack is located along a GB with misorientation angle > 15°.

3.5. Microsegregation

Fig. 4(a) shows an APT reconstruction from the as-LPBF-processed MAD542 alloy and in particular from the interdendritic regions as shown in Fig. 3, aiming to study the local chemical concentration. The APT reconstruction contains the dendritic, interdendritic regions and metastable carbides. The dendritic and interdendritic regions are revealed by the 2D concentration maps corresponding to the region denoted by the pink dashed rectangular in Fig. 4(a). An initial clear enrichment of Ti, Nb and Mo can be seen in Fig. 4(b–d). It is believed that these elemental variations are associated with the microsegregation behavior during the solidifica-

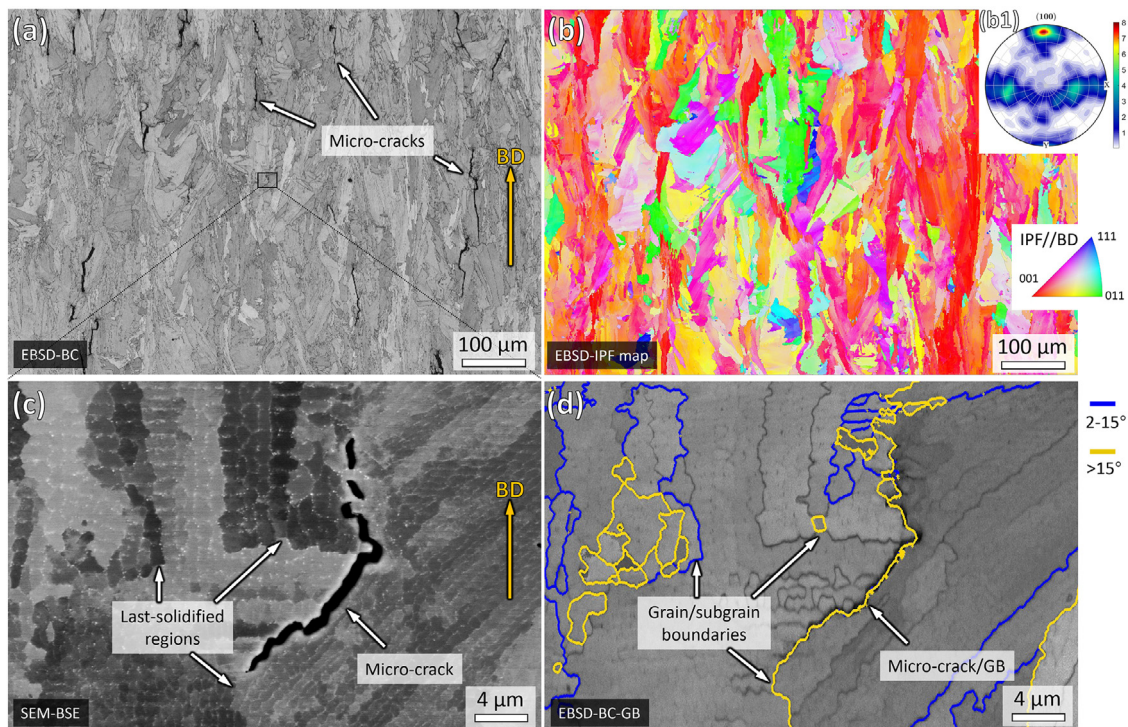


Fig. 3. (a) EBSD-BC map of the as-built MAD542 fabricated by process parameter #4, (b) EBSD-IPF coloring map of the area in (a), the coloring reference is parallel to the building direction, the inset referring to the (100) pole figure from this area, (c) SEM-BSE imaging of a micro-crack and the adjacent region, and (d) EBSD-BC map overlapped with GB plots for subgrain boundary with 2–15° misorientation and grain boundary with >15° misorientation.

tion from the LPBF process. Fig. 5 shows 1D composition profiles from a cylindrical region of interest (ROI) and along the arrow #1 shown in Fig. 4(c). Within the interdendritic region, there is a clear enrichment of Ti, Nb, Mo and Ta, while Ni and Al are depleted. There is also an enrichment of Cr and to a lesser extent of Co and C exhibit an increase within the interdendritic region.

Carbides were found to form within the enriched zone, but this was not investigated in detail since it is not within the scope of the current study. However, 1D composition profiles across the carbide are given in Fig. 6, showing that they are enriched in Mo, Cr, Ti, Ta, Nb, and W and depleted in Ni, Co, and Al, without their stoichiometry corresponding to any of the typical carbides often observed in superalloys, such as MC, $M_{23}C_6$ or M_6C . Then, the abnormal depletion of Al observed at the interdendritic region (Fig. 5) is likely due to the rejection of Al atoms when the metastable carbides are forming. It should be mentioned here that there is no ‘pile-up’ of Al concentration at the carbide/ γ interface. It is likely due to the fast-diffusing nature of Al at the elevated temperature. Here we estimate the diffusion distance, X , as the square root of the product of interdiffusion coefficient and the diffusion time. Taking the interdiffusion coefficient of Al as 2.2×10^{-14} m²/s in a Ni-7.5Al-9Cr (at.%) [50] system at 1100°C, a 10^{-3} s cumulative diffusion time leads to a diffusion distance $X=4.7$ nm. It indicates that the thermal input from the reheating of the adjacent area will reduce the elemental enrichment along the profile. It is also worth noting that, owing to the reheating of the layer-by-layer process, the significance of the microsegregation is underestimated.

Additionally, the formation of carbides is likely accelerated by the intrinsic reheating phenomena of the LPBF process during the fusion of the adjacent layers/regions. In addition, the high dislocation density locating at the interdendritic region acts as the preferred sites for carbides formation [51].

According to the APT results, the elemental segregation between the dendrite core and interdendritic region could not be suppressed during the LPBF process. In fact, the element segre-

gation in the as-LPBF-processed microstructure was also reported in detail by using high-resolution composition measurement techniques, e.g. transmission electron microscopy (TEM) Energy Dispersive X-ray Spectroscopy (EDS), in LPBF CM247LC [53] and IN718 superalloys [54].

3.6. Suppression of γ' in LPBF

Owing to the rapid cooling rate of the LPBF process, the formation of γ' precipitates is highly suppressed. Fig. 7 shows an APT reconstruction from the dendritic region of the as-LPBF-processed MAD542 superalloy alongside a corresponding frequency distribution analysis. In particular, the corresponding binomial, i.e. random, distribution is plotted to allow for comparison with the experimental distribution of the elements of Ni, Al, Cr. It can be seen that the experimental distribution for all three elements follows the binomial distribution, indicating that the solutes are randomly distributed. Thus, the observed microstructure corresponds to a super-saturated γ matrix. The high suppression of γ' in as-LPBF-processed materials is also reported for a wide range of γ' strengthened nickel-based superalloys including IN738 [52], Haynes 282 [55] and ABD-900AM [24] based on various different characterization techniques such as SEM, scanning transmission electron microscopy (STEM), and X-ray synchrotron diffraction. The APT results confirm the absence of γ' in the as-built super-saturated solid solution. The composition of the γ matrix corresponding to the APT reconstruction from Fig. 7, is given in Table 3.

However, particularly in the LPBF CM247LC superalloy, a small amount of γ' may occur in the as-built microstructure. Wang et al. [56] observed γ/γ' eutectic from dark-field TEM micrograph. The occurrence of γ/γ' eutectic is along the interdendritic region where the γ' forming elements are enriched. In the eutectic regions, the volume fraction of γ' is approximately 1.5%, according to the statistical determination from Wang et al. [56]. In addition, Divya et al. [57] observed very fine γ' in the as-built CM247LC super-

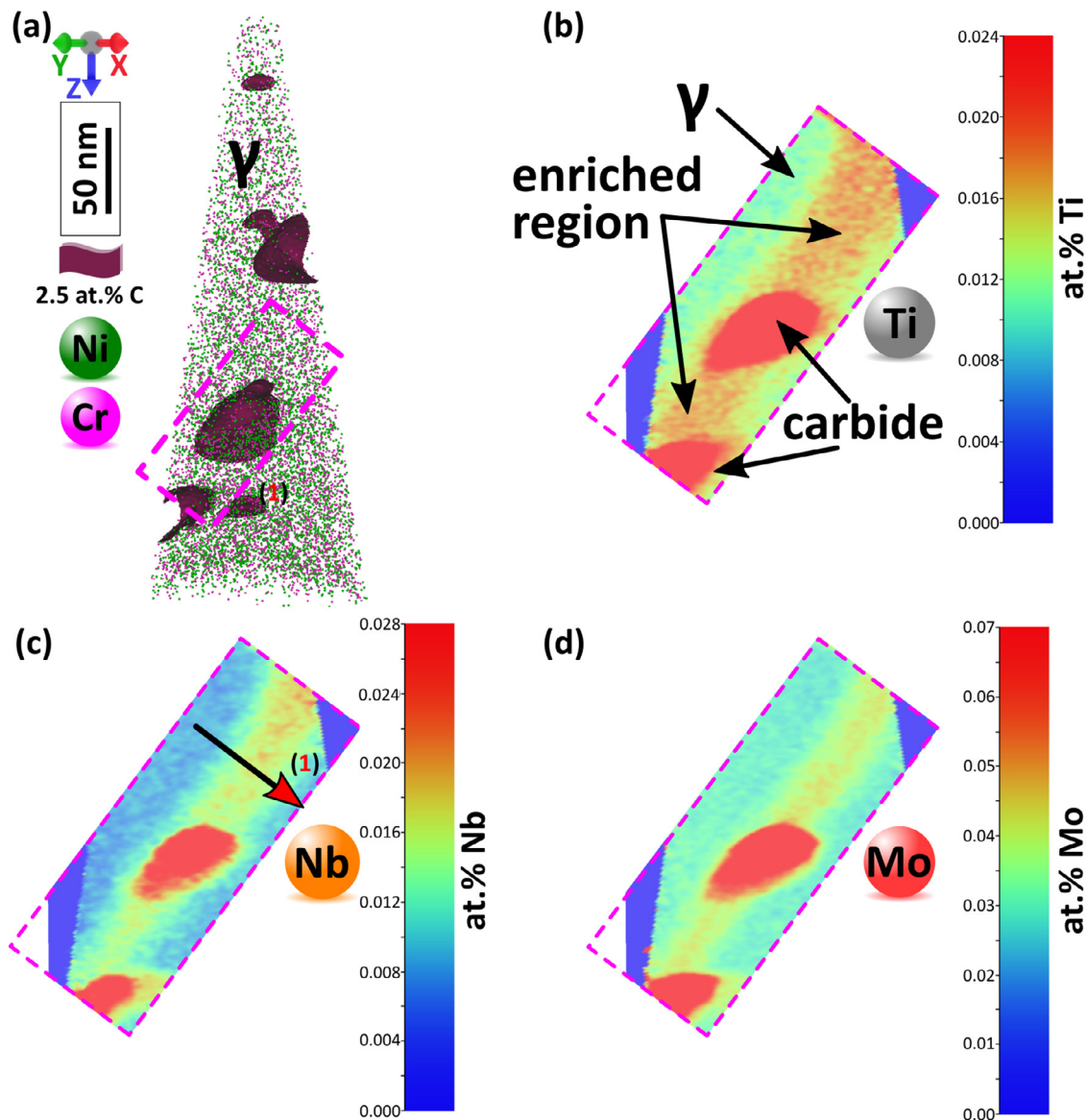


Fig. 4. (a) APT reconstruction from the MAD542 alloy from an interdendritic region containing metastable carbides. Carbides are shown with an iso-concentration surface of 2.5 at.% C. (b–d) 2D concentration maps of Ti, Nb and Mo corresponding to the region denoted by the pink rectangular box.

Table 3
Composition of MAD542 superalloy in as-built condition from dendritic region, extracted from atom probe reconstruction in Fig. 7.

	Cr	Co	Mo	W	Al	Ti	Ta	Nb	C	Ni
at.%	9.2±0.006	9.4±0.006	3.2±0.004	2.1±0.004	10.8±0.007	1.1±0.003	0.6±0.002	0.9±0.002	0.1±0.0004	62.3±0.010
wt.%	8.1±0.004	9.3±0.005	5.2±0.006	6.5±0.012	4.9±0.003	0.9±0.002	1.8±0.006	1.4±0.003	0.02±0.0001	62.6±0.069

alloy from the Moiré fringes of high-resolution TEM micrograph, where those very fine γ' are approximately 5 nm in diameter. This is likely attributed to 1) the different detailed thermal history during the LPBF process and 2) the high propensity of γ' formation of the CM247LC superalloy which has a very high equilibrium γ' volume fraction in the range of 67%.

4. Additive manufacturability diagram for nickel-based superalloys

According to the findings in the previous section, the cracking susceptibility is associated with the resistances of liquid-state and solid-state cracking. According to the existing models con-

sidering solidification cracking susceptibility as introduced in the background section, the key index parameter is the solidification range of the alloy. To some extent, this single parameter shows good qualitative predictions. To utilize this knowledge, lowering the interdendritic segregating elements is a practical way to narrow down the solidification range. Griffiths et al. [53], removed the element Hf in the CM247LC superalloy and significantly improved additive manufacturability, compared to the original CM247LC as a reference. Hf is a strong interdendritic segregating element and meanwhile a strong solidus temperature reducer. As calculated by Griffiths et al. [53], the liquidus temperatures of Hf-free CM247LC and original CM247LC are 1394 and 1383°C, respectively, indicating the limited influence on liquidus. By contrast, there is a signif-

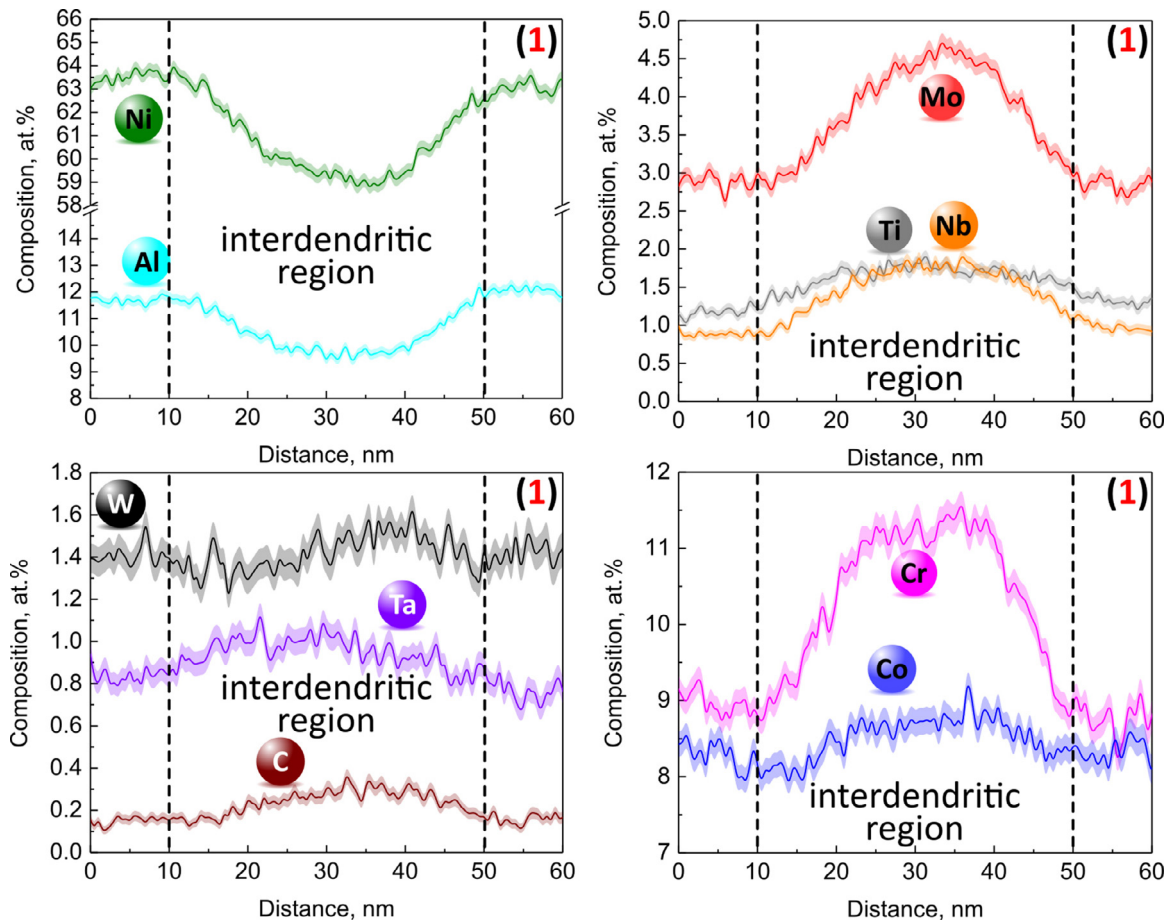


Fig. 5. 1D composition profiles from a cylindrical region of interest along the arrow #1 in Fig. 4(c). Error bars are shown as lines filled with color and correspond to the 2 σ counting error.

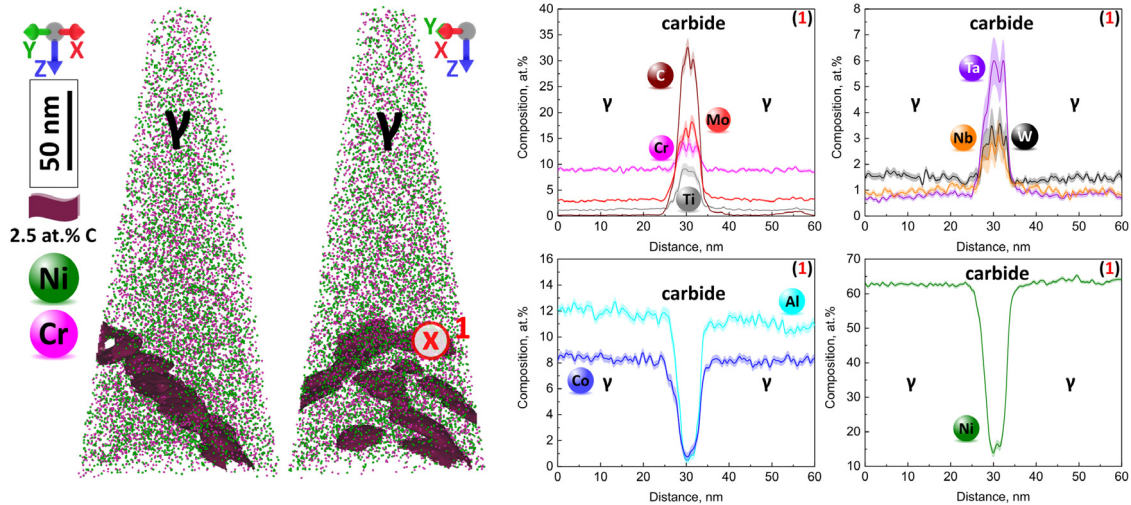


Fig. 6. APT reconstruction from the as-built MAD542 alloy from a region containing metastable carbides and the corresponding 1D composition profiles from a cylindrical region of interest along the direction pointed as #1 crossing a metastable carbide.

icant difference in the case of the solidus temperatures, which are 1241 and 858°C for Hf-free and original CM247LC, respectively. For this case, both the solidification range model by Flemings [15], and the cracking susceptibility coefficient model by Clyne and Davies [18] would give a rationalized interpretation. However, the limitation of these approaches appears when comparing a relatively wide range of superalloy grades. For example, summarized from

the solidification range results from Tang et al. [49], the IN625 and IN738LC superalloy share almost the same value of solidification ranges, but the additive manufacturability of these two alloys are far different.

Therefore, to further generalize the solidification cracking susceptibility, the mismatch of the solidification steps of the dendritic and interdendritic regions needs to be more applicable. In

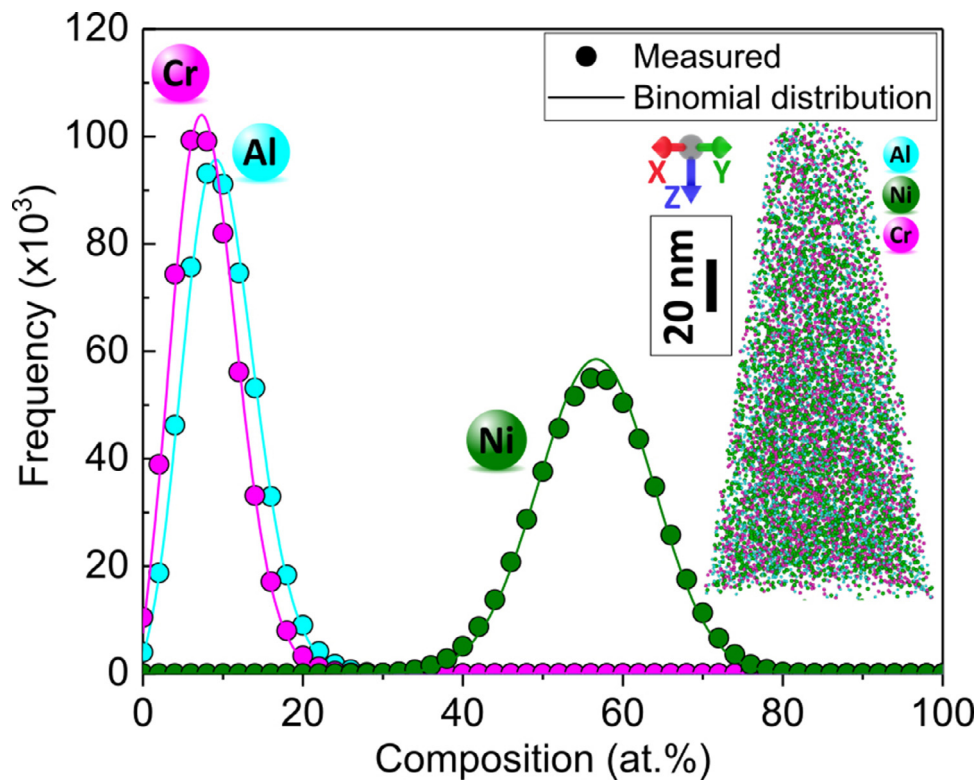


Fig. 7. APT reconstruction from the dendritic region of the as-LPBF-processed MAD542 superalloy, alongside frequency distribution analysis of Ni, Cr and Al for the same data.

the solidification process, the central issue is the mismatch of the solidus temperature between the dendritic and interdendritic regions. This statement could also be interpreted as the liquation cracking susceptibility. The liquation cracking occurs owing to the lower solidus point in the interdendritic region, which induce liquation. If the interdendritic region has a solidus temperature close to the dendrite core, the liquation would not be induced.

Regarding solid-state cracking, it is caused by the poor deformation resistance within the interdendritic region which appears as the weaker region where crack propagation occurs. It should be mentioned here, that the interdendritic region includes the high-angle GBs which are susceptible to cracking, and low-angle GBs, and the region with identical orientation between the adjacent dendrites. Even though the typical solid-state cracking, i.e., strain-age cracking and ductility dip cracking, are not commonly found during the LPBF fabrication of nickel-based superalloy, the solid-state cracking could be mixed with the liquid-state cracking.

4.1. Heat resistance and deformation resistance (HR-DR) model

Based on the understanding of the cracking mechanisms of nickel-based superalloys during the LPBF process, the last-stage solidified region is a vulnerable place which has a high susceptibility for cracking. To simply formulate the model, a 'composite-like' material is assumed, as illustrated in Fig. 8(a). In Fig. 8(a), the dendritic core (DC) region and interdendritic (ID) region are considered as two alloy substances with different chemical compositions according to the estimation from the elemental segregation behaviors. It should be highlighted here, that the ID region was simply used as the representative of the last-solidified region, where it was assumed to share the same composition of the high-angle grain boundary with high crack susceptibility. Direction Z is parallel to the solidification direction. Generalized from the cracking mechanisms, the in-process induced cracking originates from a low

resistance against heating (liquid-state cracking) and a low resistance against deformation (solid-state cracking) in the ID regions. Therefore, we propose a two-parameter-based Heat Resistance and Deformation Resistance (HR-DR) model to derive the LPBF manufacturability of nickel-based superalloys. To this sense of normalization, the idea is to compare the HR-DR difference between the ID and DC regions.

In this concept, the solute redistribution has been simplified. As illustrated in Fig. 8(b), the concentration of solute typically varies along the advancing solidification front. For simplification, two constant solute concentrations, C_{DC} and C_{ID} , are allocated to DC and ID, as illustrated in Fig. 8(c). Therefore, the area under the curve in the DC/ID regions is equal in Fig. 8(b) and (c).

To demonstrate the partitioning characteristics of alloying elements under various solidification conditions, an assumed experimental composition of nickel-based superalloy has been utilized. The composition consists of Ni-8Cr-8Co-5Mo-4W-5Al-1Ti-3Ta-2Nb-2Fe-1Hf-0.07C-0.01B-0.02Zr-0.06Si. The simulations are conducted by using Thermo-Calc 2022a software with TCNI10 and MOBNI5 databases. The solute concentration in the γ phase as a function of the mass fraction of the solid is plotted in Fig. 9. The calculated solute concentrations are directly plotted for a mass fraction up to 0.85 as solid curves, thereafter, fitted curves using a polynomial function are presented as dashed curves. A classic Scheil solidification is shown in the left column, indicating the redistribution behaviors of alloying elements during solidification at relatively low cooling rate. However, during a rapid solidification process, such as LPBF, the change of solute concentration can be progressively reduced, resulting in significantly different microsegregation profiles from the equilibrium condition [58,59]. Thereafter, two 'solute trapping' cases have been calculated under the laser scanning velocity, v , of 10^{-4} m/s and 1.0 m/s in the middle and right column in Fig. 9, respectively. The corresponding solidification rate can then be expressed as the product of v and $\cos\theta$ [60], where θ is the an-

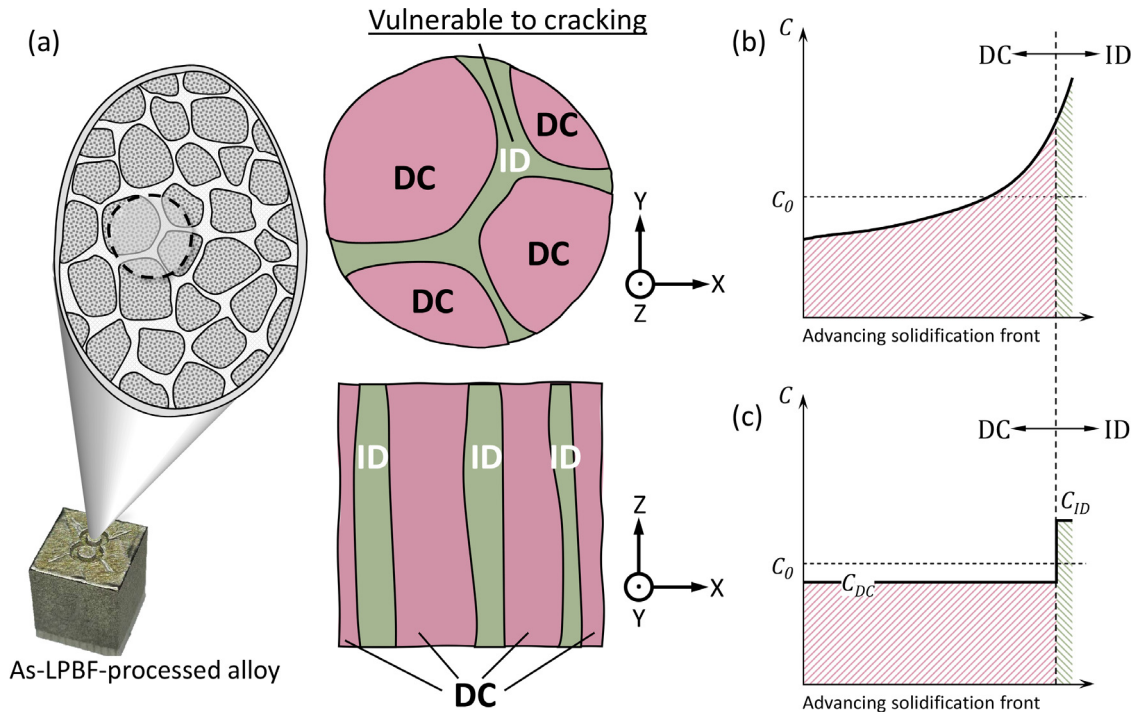


Fig. 8. (a) Schematic illustration of a unit volume during solidification, the DC indicates the dendritic core region while ID indicates the interdendritic region. Z is the direction of solidification. (b) schematic illustration of the solute profile during solidification, and (c) schematic illustration of the simplified solute profile.

gle between the heat flow direction and laser scanning direction. The θ angle is taken as 45° in the calculations (then $\cos\theta = 0.707$). The solidification rate in the orders of 10^{-4} m/s and 1.0 m/s corresponds to the practical solidification rates of directional solidification process for single-crystal superalloy production [61] and LPBF process, respectively.

Three types of elemental partitioning behaviors can be found. First, certain alloying elements such as Cr, Al, and Fe, show relatively flat profiles indicating a weak partitioning preference. Second, elements like Co and W are found enriched at the dendrite core. Third, elements like Mo, Ta, Nb, Ti, Hf, Si, C, Zr, and B partition to the interdendritic region. It should be noted that the depletion of C from the simulated profile is caused by the formation of carbides that reduces the C concentration in the γ phase. Furthermore, solidification rate dependent microsegregation behavior can be observed. For the solidification rate in the 10^{-4} m/s order, negligible solute trapping is observed. However, under the rapid solidification condition with laser scanning velocity of 1.0 m/s, for each identical element, the according profile is more flattened. The alteration of the partitioning coefficient is also significantly noticeable. For example, the equilibrium partitioning coefficient of interdendritic partitioning element B is increased by a factor of 32, comparing to the classic Scheil condition.

For the given nominal chemical composition of an alloy, the local composition of the ID and DC regions has to be determined separately as a first step. Here, a parameter named as dendrite core distribution coefficient, K_{DC/C_0}^i , has been defined as the ratio of dendrite core concentration over the nominal concentration for ith element as:

$$K_{DC/C_0}^i = \frac{C_{DC}^i}{C_0} \quad (1)$$

As illustrated in Fig. 8(b, c), the simplified C_{DC}^i can be calculated from solving the integration:

$$\int_0^{f_{DC}} C_s(f) df = \int_0^{f_{DC}} C_{DC} df = C_{DC} f_{DC} \quad (2)$$

Where f is the solid fraction, and $C_s(f)$ is the solid fraction dependent solid composition, and f_{DC} is DC fraction. In this study, f_{DC} is taken as 70% as the DC volume fraction, where 30% is used as the ID fraction f_{ID} . This assignment corresponds very well to the DC and ID fractions determined via image analysis from the previous investigation [62] in an area fraction manner. Furthermore, among different nickel-based superalloys in the as-LPBF-processed state (see Fig. S1 in the supplementary materials for the as-built IN738LC, CM247LC, MAD542, and ME3 superalloys), approximately 70% area fraction for DC were revealed by the chemical etching process. However, the chemical etching process highly depends upon the localized chemical reactivity. Considering there is no distinct boundary between DC and ID regions, the determination of 70% volume fraction for DC and the remaining 30% for ID is a reasonable approximation which is appreciated to simplify the processing of this model. It should be also highlighted here that, the presumably $f_{DC} = 70\%$ is equivalent to 94.4% of the ratio of distance from the cell core (r) by the half of dendrite arm spacing ($\lambda/2$) in an assumed hexagonal cross-section of cellular dendrite [63]. By inserting 94.4% as the one-dimensional DC solidification front and the average cellular size as 420 nm (determined in Ref. [43]) for LPBF MAD542 superalloy, it results in an ID region of approximately 23.5 nm (slight margin of $r > \lambda/2$ neglected), which is consistent with the observation of the typical cellular boundary thickness (~ 30 nm) for LPBF superalloy [52].

Fig. 10 shows the plots of C_{DC} as a function of the corresponding nominal composition C_0 . The C_{DC} is determined by the integral (Eq. (1)) from calculated composition profiles via solute trapping considered Scheil solidification of a wide group of superalloys fabricated by LPBF including AD730 [64], CM247LC [28,37,53,57,65-69], ExpAM [66], HastelloyX [70-72], Haynes 282 [55,73], IN738LC [52,74-79], IN939 [49], MAD542 (this study), NiCrAlTi [80], and Nimonic 263 [81], with various laser scanning velocity from 0.1 m/s [81] to 1.3 m/s [68].

After determination of DC composition, the ID composition, C_{ID}^i , is calculated by using a 'lever-rule' like averaging procedure, as ex-

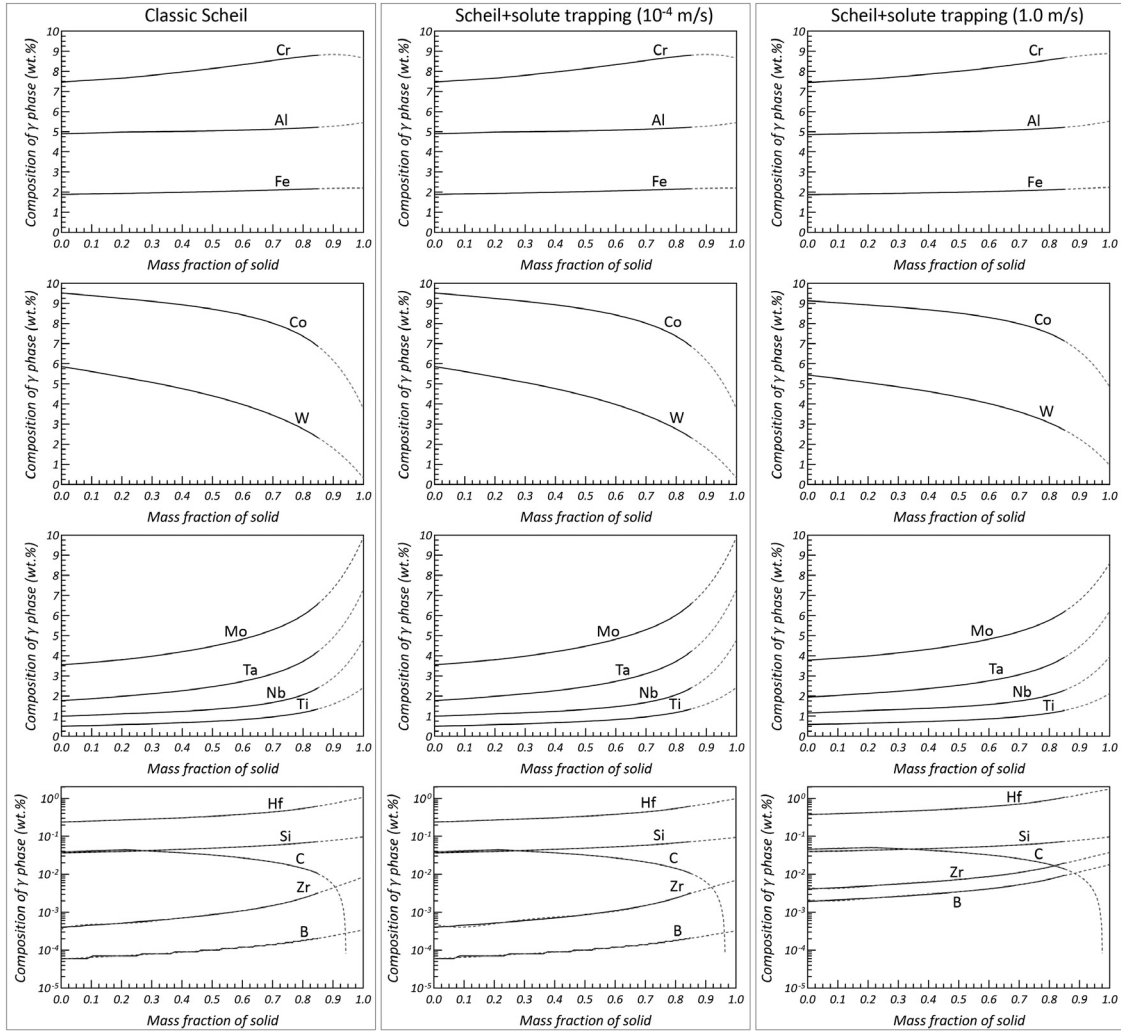


Fig. 9. Calculated solute concentration in γ phase as a function of the mass fraction of solid using classic Scheil model (left column), Scheil model considering solute trapping with laser scanning velocity of 10^{-4} m/s (middle column), and Scheil model considering solute trapping with laser scanning velocity of 1.0 m/s (right column).

Table 4
The determined dendrite core distribution coefficients of alloying elements used in this study.

Element	Cr	Co	Mo	W	Al	Ti	Ta
K_{DC/C_0}^i	0.9938	1.0655	0.8889	1.1077	0.9856	0.6911	0.7853
Element	Nb	Fe	Hf	C	B	Zr	Si
K_{DC/C_0}^i	0.6858	1.0301	0.5285	0.4914	0.2860	0.3308	0.9213

pressed as:

$$f_{DC}C_{DC}^i + f_{ID}C_{ID}^i = C_0^i \quad (3)$$

Linear regression has been made through (0,0) to determine the value of the dendrite core distribution coefficient, K_{DC/C_0}^i , for each alloying element. All the K_{DC/C_0}^i values are listed in Table 4.

4.2. Heat resistance

The first parameter, heat resistance, is formulated as the solidus temperature difference between the ID and DC substances, ΔT_S , and written as:

$$\Delta T_S = T_{S, ID} - T_{S, DC} \quad (4)$$

Here $T_{S, ID}$ and $T_{S, DC}$ is the solidus temperatures from the ID and DC composition, respectively. It should be noted here, both ID and DC are assumed as solid solutions. To calculate the solidus

temperature, in the solid solution and supersaturated solid solution of nickel-based superalloys, the solidus temperature is assumed to be a function of the gradient of solidus line of the Ni-X binary system. For example, Fig. 11 shows the calculated Ni-B binary phase diagram at the Ni rich side. With addition of B, the solidus temperature of the solid solution dramatically decreases in a nearly linear manner.

Based on this concept, the solidus temperature, T_S , is determined as follows

$$T_S = T_{Ni} + \sum_{i=1}^n G^i C^i \quad (5)$$

Where T_{Ni} is the melting point of pure Ni, and G^i are the gradients of the solidus line of the Ni- X_i binary system in the unit of $^{\circ}C/(wt.%)$, and C^i are the weight percentage of the i th element. The gradients of the solidus line of the Ni-X binary systems have

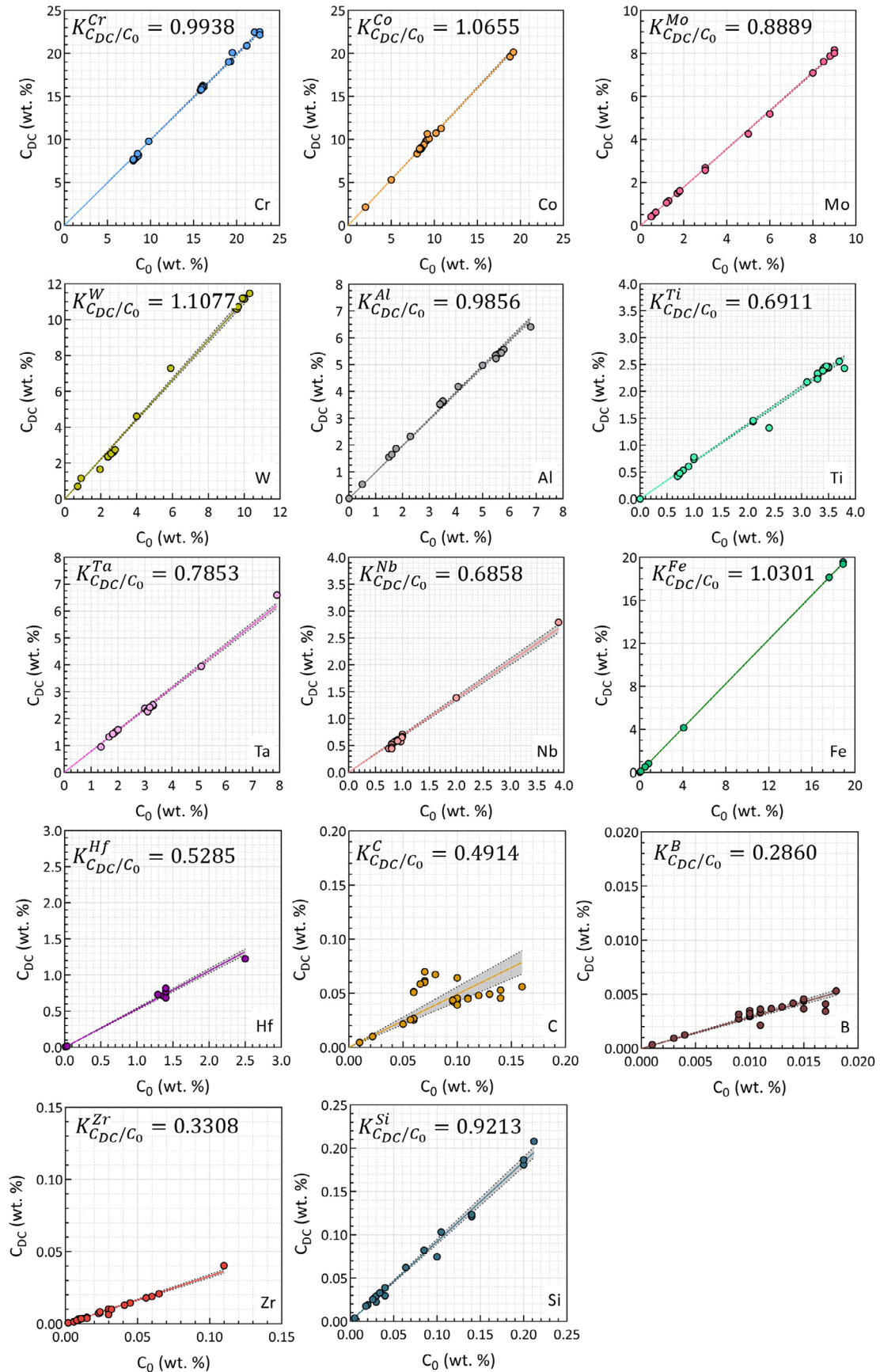


Fig. 10. The plots of C_{DC} vs. C_0 of the alloying elements including Cr, Co, Mo, W, Al, Ti, Ta, Nb, Fe, Hf, C, B, Zr, Si, in the LPBF nickel-based superalloys [28,37,49,52,53,55,57, 64–81].

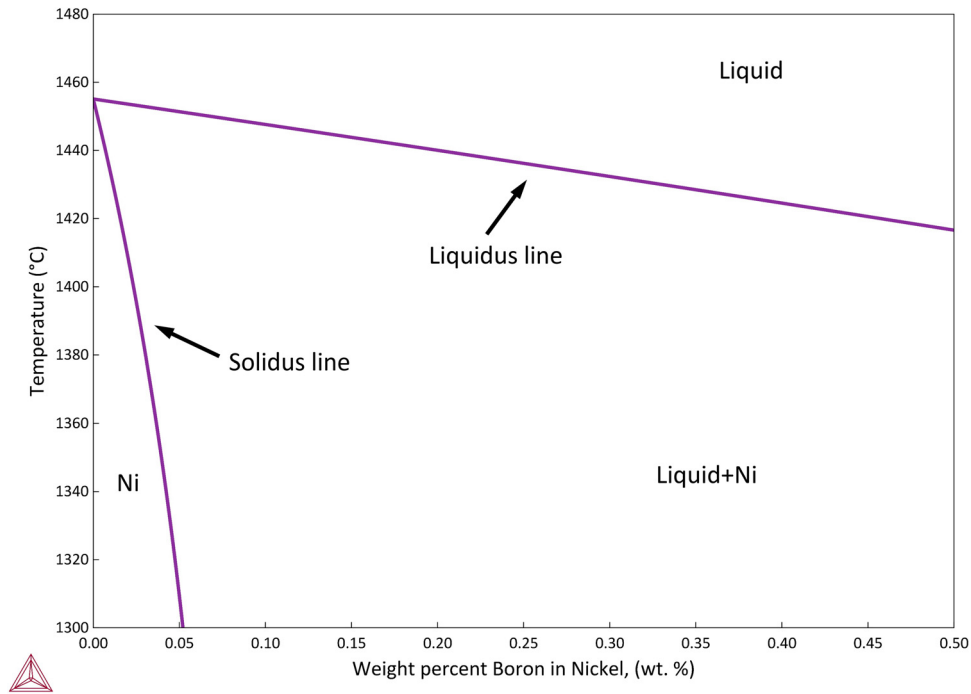


Fig. 11. Calculated Ni-B binary phase diagram with B content from 0 to 0.5 wt.% and temperature range from 1300–1480°C.

Table 5

The determined values of gradient of alloying elements on the solidus temperature from Ni-X binary system.

Element	Cr	Co	Mo	W	Al	Ti	Ta
Gradient of solidus line, G^i , (°C/wt.%)	-1.97	0.20	-0.10	2.67	-3.00	-12.20	-1.50
Element	Nb	Fe	Hf	C	B	Zr	Si
Gradient of solidus line, G^i , (°C/wt.%)	-7.67	-0.32	-73.08	-252.63	-2166.67	-588.83	-13.43

been calculated using the ThermoCalc® TCNI10 database and are summarized in Table 5.

4.3. Deformation resistance

The second parameter proposed here is the deformation resistance. Thereafter, we derive the difference of the elastic load-bearing capacities of the DC and ID substances, thus the difference in yield limit of them, $\Delta\sigma_y$, as:

$$\Delta\sigma_y = \sigma_{y, ID} - \sigma_{y, DC} \quad (6)$$

Here $\sigma_{y, ID}$ and $\sigma_{y, DC}$ is the yield strength calculated from the ID and DC composition, respectively. In the γ' -strengthened nickel-based superalloys, based on the additive law, the yield strength could be expressed using multiple individual strengthening factors [52,82], as:

$$\sigma_y = \sigma_p + \Delta\sigma_{SS} + \Delta\sigma_{GB} + \Delta\sigma_{\gamma'} + \Delta\sigma_{Dis}. \quad (7)$$

Where σ_p is the Peierls stress generated from the pure nickel lattice resistance, $\Delta\sigma_{SS}$ is the solid solution strengthening, $\Delta\sigma_{GB}$ is grain boundary strengthening, $\Delta\sigma_{\gamma'}$ is the γ' precipitation strengthening, and $\Delta\sigma_{Dis}$ is the dislocation strengthening. Here, the intention is not to quantify the absolute value of yield strength of ID and DC substances but compare the strength difference. By applying the subtraction in Eqs. (6) and (7), the σ_p is canceled out and the $\Delta\sigma_{\gamma'}$ is neglected owing to the lack of γ' . Then Eq. (7) could be rewritten as:

$$\Delta\sigma_y = (\Delta\sigma_{SS, ID} - \Delta\sigma_{SS, DC}) + (\Delta\sigma_{GB, ID} - \Delta\sigma_{GB, DC}) + (\Delta\sigma_{Dis, ID} - \Delta\sigma_{Dis, DC}) \quad (8)$$

The $\Delta\sigma_{GB}$ is considered under the basis of Hall-Petch strengthening law and is inversely proportional to the square root of grain size. Therefore, the grain size is the dominant parameter on determining the grain boundary strengthening. In the as-LPBF-processed microstructure of nickel-based superalloys, the grain size largely depends upon the LPBF process-related input parameter, resulting in that $\Delta\sigma_{GB}$ is a chemical composition weakly dependent term. According to the well-known Taylor's dislocation strengthening equation [83], the $\Delta\sigma_{Dis}$ part is proportional to the square root of dislocation density, considering the close values for material constant, shear modulus, and Taylor's factors of nickel-based superalloys. From extensive studies on the dislocation density in the as-built LPBF microstructure of different engineering alloys [52,84,85] it remains as almost a constant value, which is typically in the order of 10^{14} m^{-2} . Additionally, in the cellular forming metallic materials, the $\Delta\sigma_{Dis}$ could be considered as inversely proportional to the cellular size [86,87]. Herein, the cellular size is markedly determined by the manufacturing process and limitedly influenced by the chemical composition. As in the wide range of as-LPBF-processed nickel-based superalloy grades (e.g. LPBF IN718 [54], IN625 [88], Hastelloy X [89,90], IN939 [91], IN738LC [51], and CM247LC [57]), the average cellular interspacing is in the narrow window of 400–600 nm. For a given superalloy, the different LPBF process parameters also give a close cellular size. Based on these assumptions, the yield strength difference between ID and DC is then expressed as:

$$\Delta\sigma_y = (\Delta\sigma_{SS, ID} - \Delta\sigma_{SS, DC}) + \Delta\sigma(P) = \Delta\sigma_{SS} + Constant \quad (9)$$

Where $\Delta\sigma(P)$ is the strengthening factors determined by the LPBF process rather than the chemistry and therefore considered as a constant here. Then, the yield strength difference is primar-

Table 6
The determined solid solution strengthening coefficient of alloying elements used in this study.

Element	Cr	Co	Mo	W	Al	Ti	Ta
Solid solution strengthening coefficient, (MPa·at.frac. ^{-1/2})	337	39.4	1015	977	225	775	1191
Element	Nb	Fe	Hf	C	B	Zr	Si
Solid solution strengthening coefficient, (MPa·at.frac. ^{-1/2})	1183	153	N/A	N/A	N/A	N/A	N/A

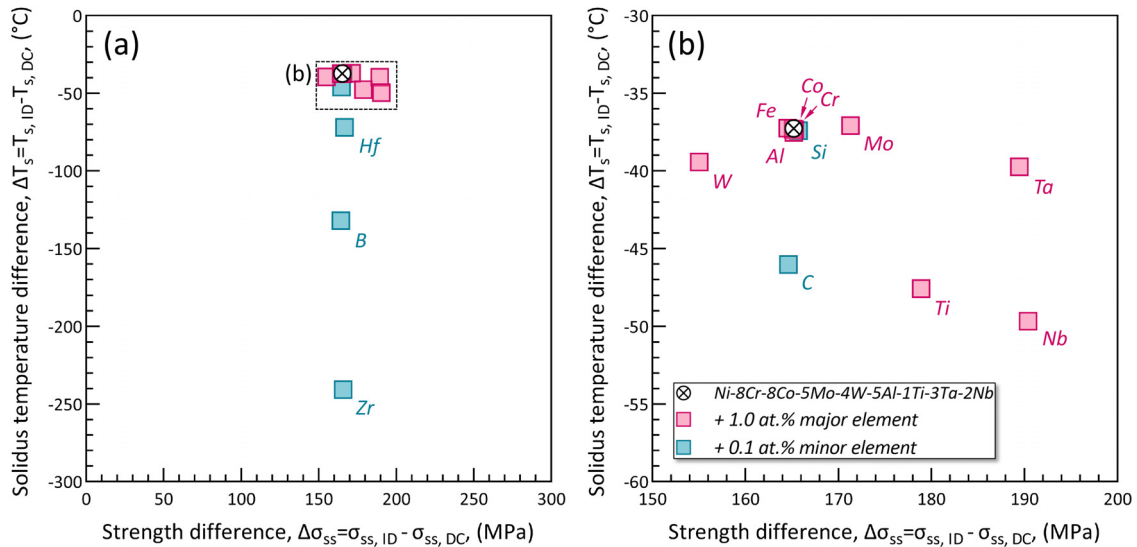


Fig. 12. (a) Elemental influence on the additive manufacturability of a Ni-8Cr-8Co-5Mo-4W-5Al-1Ti-3Ta-2Nb superalloy by increasing 1 at. % major or 0.1 at. % minor alloying elements to the nominal chemical composition, (b) enlarged view of the box (b) indicated in (a).

ily dominated by the $\Delta\sigma_{SS}$ only. For a single γ phase solid solution, as the as-LPBF-processed microstructure shows, the $\Delta\sigma_{SS}$ is determined by the alloying elements. And the solid solution strengthening difference between ID and DC is expressed as chemical composition-based equation:

$$\Delta\sigma_{SS} = (\Delta\sigma_{SS, ID} - \Delta\sigma_{SS, DC}) = \sum_{i=1}^n \sqrt{\chi_{ID}^i} \cdot \frac{d\sigma}{\sqrt{d\chi^i}} - \sum_{i=1}^n \sqrt{\chi_{DC}^i} \cdot \frac{d\sigma}{\sqrt{d\chi^i}} \quad (10)$$

Where χ_{ID}^i and χ_{DC}^i are the atomic fraction of the *i*th alloying element of the ID and DC, respectively, and $d\sigma/\sqrt{d\chi^i}$ is the solid solution strengthening coefficient for the *i*th element, which is provided in detail in references [92,93] and summarized in Table 6. For the minor elements, the solid solution strengthening is less considered in this study, because they are prone to form secondary phase in minor amount, e.g. the metastable carbides as indicated from APT results.

5. Discussion

5.1. Influence of alloying elements on printability

In the previous section, the heat and deformation resistance can be estimated for a given superalloy based on the HR-DR analysis. If one alloy shows the combination of a higher value of both ΔT_s and $\Delta\sigma_{SS}$, this alloy is expected to have better resistance to the in-LPBF-process induced cracking. To visualize this approach, the additive manufacturability diagram of nickel-based superalloy is developed, where the two parameters are assigned on the X and Y axis in an X-Y plot.

In Fig. 12, the influence of alloying elements on the additive manufacturability of a given superalloy (MAD542) is illustrated. By increasing 1 at.% of the major alloying elements, Nb, Ta, Ti, and Mo are dragging the superalloy towards higher deformation resis-

tance. These elements are considered beneficial on improving the solid-state cracking resistance. On the other hand, alloying element W reduces the ID deformation resistance, which is harmful for resisting the solid-state cracking. Other major alloying elements, like Fe, Al, Cr, Co do not show severe influence according to the HR-DR model in this study. Another type of important alloying elements heavily doped into nickel-based superalloys are the minor elements. Fig. 12 also presents the influence of minor elements by increasing 0.1 at.% to the nominal composition. Among them, Zr, B, and Hf significantly decrease the heat resistance, leading to a terrible liquid-state cracking resistance. While Si and C show less impact as illustrated in the enlarged view in Fig. 12(b).

5.2. Chemical composition window for LPBF

Inspired by the additive manufacturability diagram, the chemical composition window of nickel-based superalloys for the LPBF process can now be determined. More than 20 (see Table 7) different nickel-based superalloys and their derivative versions [28,37,49,52,53,57,64,65,67–71,73–79,81,88,90,94–107], newly developed γ' strengthened superalloys [24,49,62,66] as well as experimental nickel-based superalloys [80] and Co-Ni-based superalloys [108], fabricated by the LPBF process are integrated into the additive manufacturability diagram by implementing their chemical composition including both major and minor alloying elements. Also, the experimentally observed susceptibility to in-process cracking is identified and extracted from each study.

Fig. 13 illustrates the basic concept that the deformation and heat resistances, $\Delta\sigma_{SS}$ and ΔT_s , are plotted on the X-Y plot, respectively. As can be seen, the reported cracking conditions in the as-LPBF-processed state correlate very well with the additive manufacturability diagram. The estimated $\Delta\sigma_{SS}$ and ΔT_s , and the as-built cracking condition, and equilibrium γ' volume fraction calculated at 800°C (ThermoCalc®, TCNI10 database) are summarized and listed in Table 7. The detailed calculation procedures and full

Table 7

Summary of calculated $\Delta\sigma_{SS}$ and ΔT_S values, as-built crack conditions, and calculated γ' volume fraction (at 800°C) of superalloys in Fig. 13.

Alloy	Ref.	DR, $\Delta\sigma_{SS}$ (MPa)	HR, ΔT_S (°C)	Crack condition	γ' volume fraction (%)
AD730	[64]	121.2	-165.8	Cracked	31.5
CM247LC	[49]	55.6	-287.5	Cracked	72.8
CM247LC	[37]	53.9	-304.7	Cracked	73.7
CM247LC	[28]	54.6	-321.9	Cracked	75.8
CM247LC	[65]	54.8	-305.5	Cracked	73.7
CM247LC	[67]	53.7	-304.6	Cracked	73.7
CM247LC	[53]	53.8	-302.2	Cracked	73.6
CM247LC	[68]	58.1	-274.3	Cracked	72
CM247LC	[68]	53.2	-305.2	Cracked	73.6
CM247LC	[69]	88.1	-438.4	Cracked	81.1
CM247LC	[57]	54.9	-283.5	Cracked	71.3
CM247LC	[66]	54.8	-310.7	Cracked	72.8
CMSX486	[67]	68.0	-275.1	Cracked	74.9
IN738LC	[74]	146.2	-186.8	Cracked	47.9
IN738LC	[75]	144.0	-231.3	Cracked	47.1
IN738LC	[75]	147.2	-234.9	Cracked	48.1
IN738LC	[75]	147.2	-259.5	Cracked	48.7
IN738LC	[75]	148.8	-225.7	Cracked	48.1
IN738LC	[75]	141.6	-221.6	Cracked	47
IN738LC	[75]	147.4	-255.0	Cracked	49.6
IN738LC	[76]	146.3	-186.8	Cracked	48
IN738LC	[76]	149.0	-325.9	Cracked	47.1
IN939	[49]	131.3	-321.4	Cracked	34.6
Mar M-247	[103]	61.3	-401.0	Cracked	71.7
ME3	[105]	149.2	-378.1	Cracked	44.8
ME3	[106]	171.9	-300.4	Cracked	50.2
RENÉ 108	[109]	53.2	-192.8	Cracked	67.9
CM247LCNhf	[53]	48.4	-127.7	Nearly crack-free	69.2
ExpAM-mod	[66]	193.7	-170.5	Nearly crack-free	48.2
IN738LC	[79]	148.7	-193.8	Nearly crack-free	47.9
IN738LC	[75]	144.1	-172.3	Nearly crack-free	48
IN738LC	[75]	142.0	-210.4	Nearly crack-free	47.2
IN939	[102]	132.2	-303.0	Nearly crack-free	35.6
Nimonic 263	[81]	99.9	-32.8	Nearly crack-free	1.1
MAD542	This study	162.0	-87.9	Crack-free	61.2
ME3	This study	182.2	-112.2	Crack-free	53.1
ABD-850AM	[49]	105.7	-59.3	Crack-free	18.1
ABD-900AM	[49]	154.1	-97.9	Crack-free	30
AD730	[64]	105.9	-84.2	Crack-free	30.4
AD730	[64]	125.5	-61.8	Crack-free	34.2
ExpAM	[66]	196.9	-42.0	Crack-free	49.5
Haynes 282	[73]	100.5	-74.5	Crack-free	16.7
Haynes 282	[55]	102.4	-65.1	Crack-free	17.6
Hastelloy X	[70]	35.8	-6.2	Crack-free	0
Hastelloy X	[71]	43.4	-27.1	Crack-free	0
Hastelloy X	[90]	58.3	-101.6	Crack-free	0
Hastelloy X	[72]	34.9	-26.3	Crack-free	0
IN625	[67]	158.4	-54.0	Crack-free	0
IN625	[98]	179.9	-84.2	Crack-free	0
IN625	[88]	158.4	-76.0	Crack-free	0
IN718	[99]	174.1	-65.4	Crack-free	0
IN718	[94]	178.9	-66.5	Crack-free	1.3
IN718	[100]	174.9	-72.0	Crack-free	0
IN718	[110]	172.4	-82.3	Crack-free	0
IN738LC	[77]	148.8	-188.7	Crack-free	47.9
IN738LC	[95]	104.2	-91.1	Crack-free	45.7
IN738LC	[52]	151.6	-191.5	Crack-free	48.9
IN738LC	[78]	151.5	-195.6	Crack-free	47.9
K418	[97]	128.4	-150.8	Crack-free	65.7
K418	[111]	131.7	-84.4	Crack-free	64.9
NiCrAlTi	[80]	41.8	-13.7	Crack-free	46.8
SB-CoNi-10	[108]	67.7	-105.0	Crack-free	57.3
SRR99	[108]	64.2	-41.1	Crack-free	72.1
Rene77	[112]	99.8	-77.8	Crack-free	51.05
Rene41	[113]	116.4	-75.3	Crack-free	24.42

table including the specific composition used in the calculations are provided in Supplementary data.

Superalloys that are expected to be readily adopted for the LPBF process are expected to lean towards the top right of the diagram. Based on the experimental results in this study and from literature, the additive manufacturability boundary which determines

the chemical composition window can then also be plotted. As shown in Fig. 13(a), the cracked and crack-free superalloys by LPBF are separated by a clear boundary. It should be pointed out here, that the chemical composition window (upper right area) is estimated conservatively, since the cracking could be caused by improperly optimized printing parameters. According to the box plots

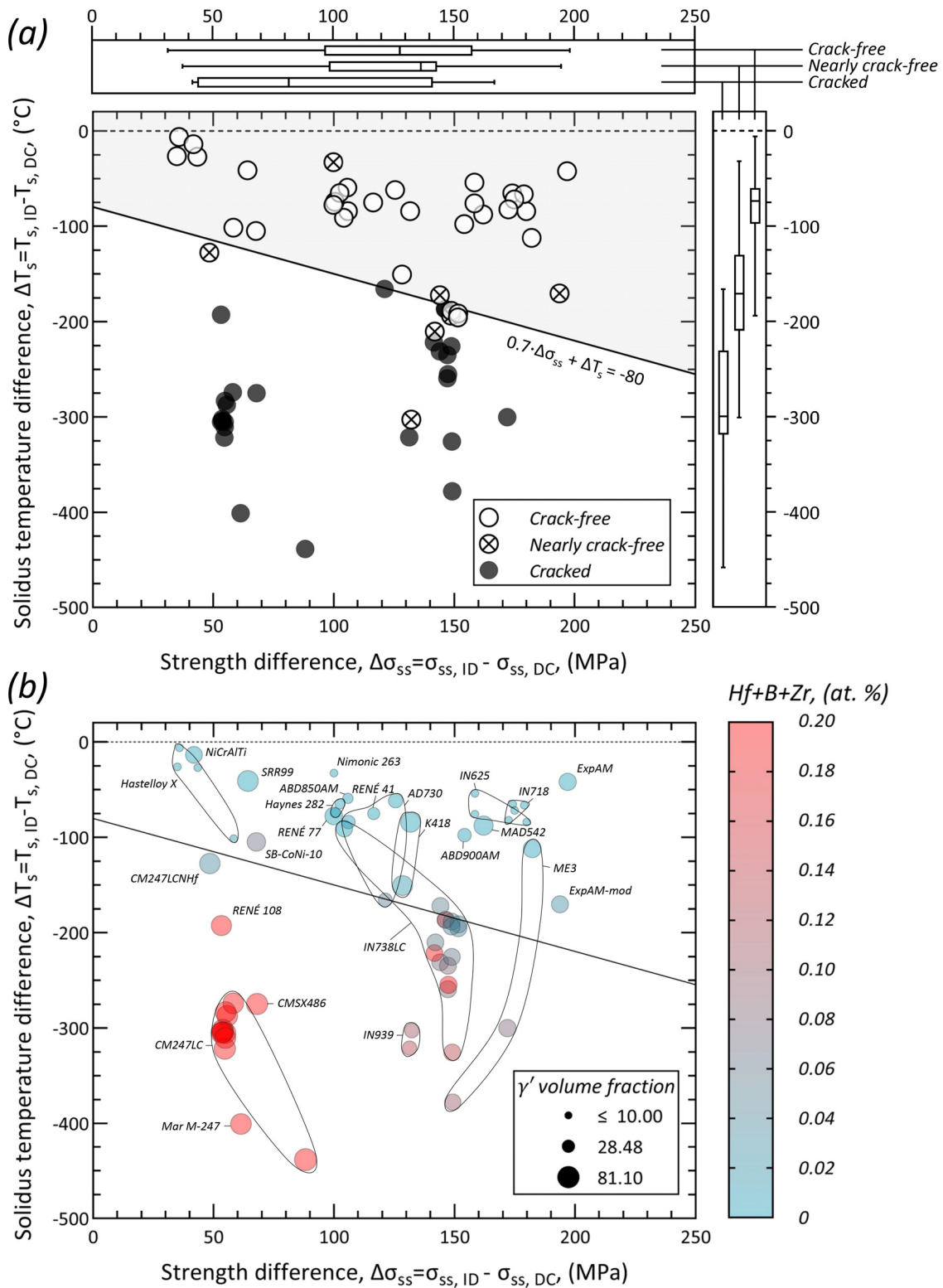


Fig. 13. (a) Additive manufacturing chemical composition window of nickel-based superalloys for LPBF based on additive manufacturability diagram, box plots of values from X and Y are shown at the top and right of the figure, where the whisker indicates the min-max. In (b), the size of marks indicates γ' volume fraction from thermodynamic calculation at 800°C, the marks are colored by the addition of the sum of Hf, B, and Zr in at.% according to the color scheme on the right-hand side of (b).

shown in Fig. 13(a), lesser discrepancies can be observed by using the HR index solely compared to using the DR index solely. The HR and DR indices are the indicators for the liquid- and solid-state cracking, respectively. And HR is more predominately determining the overall crack susceptibility, which agrees with the experimen-

tal findings that liquid-state cracking is more commonly observed (Fig. 2). However, the combined pair of HR and DR is supposed to be more predictive. Here we propose a mathematic criterion as: $0.7 \cdot \Delta \sigma_{ss} + \Delta T_s = -80$, by using the dimensionless quantities. The weight factor of 70% on the DR index is consistent with the

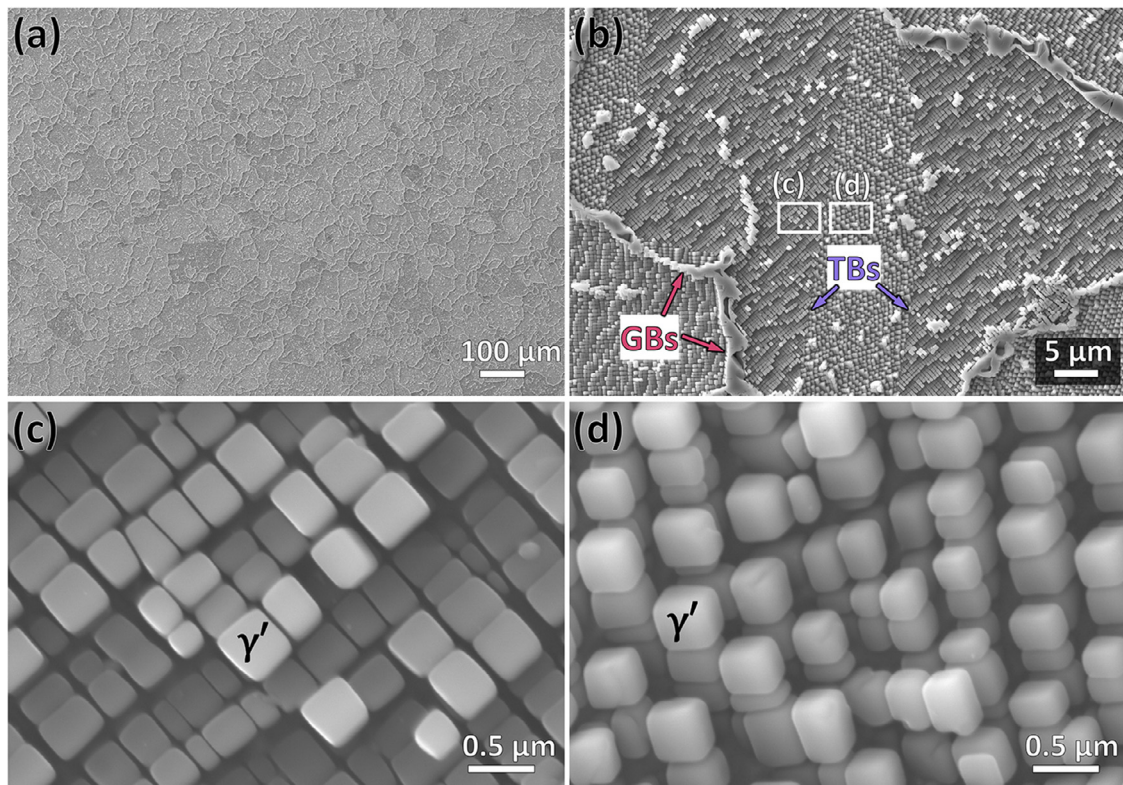


Fig. 14. SEM-SE micrographs of electro-etched LPBF MAD542 superalloy after post-processing heat treatment (a) large scale overview, (b) γ' in the grain interior, grain boundary and twin boundary, (c) γ' in the parent grain and (d) γ' in the twin.

sults that solid-state cracking is less severe than the liquid-state one.

The superalloys have relied on the minor elements for decades, and these minor elements will be needed to accomplish high-performing superalloys also in the foreseen future. From the AM perspective, these minor elements indeed influence additive manufacturability in different ways. According to Fig. 12, Hf, B, and Zr are shown to have the most detrimental effect on the cracking resistance with respect to the liquid-state cracking resistance. The sum of addition of Hf, B and Zr in at.% is used for coloring the symbols in Fig. 13(b). For a superalloy and its derivatives, the additive manufacturability is largely dependent on the amount of added minor elements. For example, the original CM247LC shows high cracking susceptibility [53]. While, by removing the Hf, Griffiths et al. [53], reported that nearly crack-free Hf-free CM247LC was achieved. Similar results are found in IN738LC and its derivatives, several research groups reported the crack-free [52,77,78,95], or nearly crack-free [75,79,101] IN738LC parts by LPBF, while cracked samples were still presented in other investigation [74]. Another superalloy illustrating differentiated additive manufacturability is the ME3. In this study, the B-free ME3 is fabricated to a crack-free quality, while the B-containing ME3 superalloys suffer from high cracking susceptibility [105,106]. The primary aspect determining the additive manufacturability of the same designation of superalloy is thus the amount of minor elements. To this scene, this diagram is expected to also provide guidelines for tailoring the minor elements in a controllable manner, which frankly results in the prediction of additive manufacturability.

5.3. Influence of γ' precipitates

In Fig. 13(b), the size of the spheres was based on the γ' volume fraction calculated in the equilibrium state at 800°C.

Clearly, the γ' phase fraction has limited influence on the additive manufacturability. High γ' (>60%) volume fraction superalloys (e.g. MAD542 in this study) could still be produced crack-free by LPBF. Fig. 14 presents the γ' morphology of the crack-free MAD542 superalloy by LPBF. The γ' precipitates are developed after post-processing heat treatment: 1230°C/2h, 1080°C/4h, 900°C/24h. Fig. 14(a) shows the large-scale viewing of SEM micrograph presenting the crack-free microstructure. In Fig. 14(b), extensive and high-volume fraction of γ' precipitates are observed. In this heat-treated condition, the volume fraction of γ' is up to 65%. Coarse γ' are located at the GBs, and finer γ' are embedded in the grain interior. No coarse and abnormal shaped γ' are found at the coherent twin boundaries (TBs). Fig. 14(c, d) presents the morphology of γ' in MAD542 superalloy from detailed SEM micrographs. After post-processing heat treatment, the γ' is developed into a cuboidal shape with round corners and a size of 200–500 nm.

For decades, the nickel-based superalloy welding community have been using the Prager and Shira's diagram to predict the weldability, in particular the susceptibility to strain age cracking [114]. By considering the sum of Al (wt.%) + 0.5 × Ti (wt.%) equals to 3 wt.% as the critical boundary to separate the superalloys into weldable and non-weldable ones with respect to the strain aging cracking. The elements Al and Ti are the two principal γ' formers, and undoubtedly higher Al and Ti alloys show greater γ' phase formation propensity. However, LPBF is a manufacturing process that suppress the formation of γ' , i.e., γ' phase is barely observed in the as-built superalloys (Fig. 7). Therefore, non-weldable superalloys are not equivalent to non-additive manufacturable superalloys. In this study, the weight percentage of Al + 0.5 × Ti is 5.5 wt.% and 5.45 wt.% for MAD542 and ME3, respectively, which is apparently greater than the 3 wt.% boundary for the weldability criteria. But both MAD542 and ME3 have been proven to be pos-

sible to fabricate in a crack-free condition by LPBF (Fig. 1). This is similar to the results from other studies on newly developed γ' strengthened nickel-based superalloys, like ABD-850AM, ABD-900AM [24,49], ExpAM [66] with high γ' volume fraction which could be fabricated crack-free as well. Under this basis, the LPBF process provides a great opportunity for superalloys, especially γ' strengthened superalloys, to be further developed. The HR-DR model as well as the additive manufacturability diagram approach proposed in this work offers a reliable tool for alloy design.

6. Summary and conclusions

The additive manufacturability of nickel-based superalloys for laser powder bed fusion is investigated in this study. The following conclusions can be drawn:

- (1) A two-parameter-based model, considering heat resistance and deformation resistance (HR-DR), was formulated to predict the additive manufacturability. An additive manufacturability diagram was established based on the HR-DR analysis to visualize the suitable chemical composition window of nickel-based superalloy for the LPBF process. The HR-DR model and the additive manufacturability diagram show excellent consistency with the experimental results.
- (2) According to the HR-DR model, minor elements, Zr, B, and Hf dramatically reduce the cracking resistance of a nickel-based superalloy when fabricated by LPBF, while the equilibrium γ' volume fraction shows limited influence on the additive manufacturability.
- (3) The γ' strengthened nickel-based superalloys, MAD542 and ME3, have been fabricated in a crack-free condition by LPBF. The success of printing these alloys validates the HR-DR model experimentally.
- (4) In the as-built microstructure of the MAD542 alloy, enrichment of Ti, Nb, Mo and Ta is observed at the interdendritic regions. Ni and Al were found to be deplete in these regions, as revealed by atom probe tomography. The elemental microsegregation behaviors allow the as-built microstructure to be assumed as 'composite-like' material for formulating the model.
- (5) In the as-LPBF-processed microstructure of the MAD542 alloy, the formation of γ' phase is highly suppressed as revealed by atom probe tomography. Thus, a supersaturated solid solution γ phase is obtained in the as-built microstructure. This unique microstructural feature simplifies the calculations in the HR-DR model.
- (6) The illustrated HR-DR analysis and the additive manufacturability diagram is beneficial for guiding the alloy development approach of nickel-based superalloy for LPBF process.

Declaration of Competing Interest

No potential conflict of interest was reported by the authors.

Acknowledgments

This work was supported by the Swedish Agency for Innovation Systems via SIP Metalliska Material, (Vinnova grant 2018-00804); faculty grant from Linköping University (SFO-MAT-LiU#2009-00971); and CAM2 the Center for Additive Manufacture – Metal (Vinnova grant 2016-05175). Dr. Hans Gruber and Chalmers University of Technology is acknowledged for fabricating the LPBF MAD542 and ME3 alloys. Uwe Tezins and Andreas Sturm are acknowledged for their support to the FIB and APT facilities at MPIE.

Supplementary materials

Supplementary material associated with this article can be found, in the online version, at doi:10.1016/j.actamat.2022.118307.

References

- [1] J.H. Martin, B.D. Yahata, J.M. Hundley, J.A. Mayer, T.A. Schaedler, T.M. Pollock, 3D printing of high-strength aluminium alloys, *Nature* 549 (2017) 365–369, doi:10.1038/nature23894.
- [2] E. Chauvet, P. Kontis, E.A. Jäggle, B. Gault, D. Raabe, C. Tassin, J.J. Blandin, R. Dendievel, B. Vayre, S. Abed, G. Martin, Hot cracking mechanism affecting a non-weldable Ni-based superalloy produced by selective electron beam melting, *Acta Mater.* 142 (2018) 82–94, doi:10.1016/j.actamat.2017.09.047.
- [3] T.M. Pollock, S. Tin, Nickel-based superalloys for advanced turbine engines: chemistry, microstructure and properties, *J. Propuls. Power.* 22 (2006) 361–374, doi:10.2514/1.18239.
- [4] R.C. Reed, *The Superalloys Fundamentals and Applications*, Cambridge University Press, Cambridge, 2006.
- [5] M.C. Hardy, B. Zirbel, G. Shen, R. Shankar, Developing damage tolerance and creep resistance in a high strength nickel alloy for disc applications, in: Proceedings of the International Symposium on Superalloy, 2004, pp. 83–90, doi:10.7449/2004/superalloys_2004_83_90.
- [6] T. Murakumo, T. Kobayashi, Y. Koizumi, H. Harada, Creep behaviour of Ni-base single-crystal superalloys with various γ' volume fraction, *Acta Mater.* 52 (2004) 3737–3744, doi:10.1016/j.actamat.2004.04.028.
- [7] F.T. Furillo, J.M. Davidson, J.K. Tien, L.A. Jackman, The effects of grain boundary carbides on the creep and back stress of a nickel-base superalloy, *Mater. Sci. Eng.* 39 (1979) 267–273, doi:10.1016/0025-5416(79)90065-X.
- [8] G.B. Viswanathan, P.M. Sarosi, M.F. Henry, D.D. Whitis, W.W. Milligan, M.J. Mills, Investigation of creep deformation mechanisms at intermediate temperatures in René 88 DT, *Acta Mater.* 53 (2005) 3041–3057, doi:10.1016/j.actamat.2005.03.017.
- [9] P. Kontis, H.A.M. Yusof, S. Pedrazzini, M. Danaie, K.L. Moore, P.A.J. Bagot, M.P. Moody, C.R.M. Grovenor, R.C. Reed, On the effect of boron on grain boundary character in a new polycrystalline superalloy, *Acta Mater.* 103 (2016) 688–699, doi:10.1016/j.actamat.2015.10.006.
- [10] N. Wang, S. Mokadem, M. Rappaz, W. Kurz, Solidification cracking of superalloy single- and bi-crystals, *Acta Mater.* 52 (2004) 3173–3182, doi:10.1016/j.actamat.2004.03.047.
- [11] J. Zhang, R.F. Singer, Hot tearing of nickel-based superalloys during directional solidification, *Acta Mater.* 50 (2002) 1869–1879, doi:10.1016/S1359-6454(02)00042-3.
- [12] C.E. Cross, On the origin of weld solidification cracking, in: *Hot Cracking Phenomena in Welds*, Springer-Verlag, 2005, pp. 3–18.
- [13] D.G. Eskin, L. Katgerman, A quest for a new hot tearing criterion, *Metall. Mater. Trans. A* 38 (2007) 1511–1519, doi:10.1007/s11661-007-9169-7.
- [14] I. Farup, J.M. Drezet, M. Rappaz, *In situ* observation of hot tearing formation in succinonitrile-acetone, *Acta Mater.* 49 (2001) 1261–1269, doi:10.1016/S1359-6454(01)00013-1.
- [15] M.C. Flemings, *Solidification Processing*, McGraw-Hill College, New York, 1974.
- [16] T. Böllighaus, H. Herold, C. Cross, J.C. Lippold, *Hot Cracking Phenomena in Wels II*, Springer, 2008.
- [17] V. Shankar, T.P.S. Gill, S.L. Mannan, S. Sundaresan, Criteria for hot cracking evaluation in austenitic stainless steel welds using longitudinal varendstraint and transvarendstraint tests, *Sci. Technol. Weld. Join.* 5 (2000) 91–97, doi:10.1179/136217100101538074.
- [18] G.J. Clyne, T.W. Davies, A quantitative solidification cracking test for castings and an evaluation of cracking in aluminium-magnesium alloys, *British Foundryman* 68 (1975) 238–244.
- [19] M. Rappaz, J.M. Drezet, M. Gremaud, A new hot-tearing criterion, *Metall. Mater. Trans. A* 30 (1999) 449–455, doi:10.1007/s11661-999-0334-z.
- [20] D. Raabe, M. Herbig, S. Sandlöbes, Y. Li, D. Tytko, M. Kuzmina, D. Ponge, P.P. Choi, Grain boundary segregation engineering in metallic alloys: a pathway to the design of interfaces, *Curr. Opin. Solid State Mater. Sci.* 18 (2014) 253–261, doi:10.1016/j.cossms.2014.06.002.
- [21] J. Grodzki, N. Hartmann, R. Rettig, E. Affeldt, R.F. Singer, Effect of B, Zr, and C on hot tearing of a directionally solidified nickel-based superalloy, *Metall. Mater. Trans. A* 47 (2016) 2914–2926, doi:10.1007/s11661-016-3416-8.
- [22] S. Kou, *Welding Metallurgy*, Second Edition S. Edition, S. Edition, S. Kou, S. Edition, S. Kou, S. Edition, John Wiley & Sons, Inc., Hoboken, NJ, USA, 2003 10.1016/j.theochem.2007.07.017.
- [23] O.A. Ojo, N.L. Richards, M.C. Chaturvedi, Contribution of constitutional liquation of gamma prime precipitate to weld HAZ cracking of cast Inconel 738 superalloy, *Scr. Mater.* 50 (2004) 641–646, doi:10.1016/j.scriptamat.2003.11.025.
- [24] Y.T. Tang, J.N. Ghousoub, C. Panwisawas, D.M. Collins, S. Amirkhanlou, J.W.G. Clark, A.A.N. Németh, D. Graham McCartney, R.C. Reed, The effect of heat treatment on tensile yielding response of the new superalloy ABD-900AM for additive manufacturing, in: *The Minerals, Metals & Materials Series*, Springer, Cham, 2020, pp. 1055–1065.
- [25] P. Kontis, E. Chauvet, Z. Peng, J. He, A.K. da Silva, D. Raabe, C. Tassin, J.J. Blandin, S. Abed, R. Dendievel, B. Gault, G. Martin, Atomic-scale grain boundary engineering to overcome hot-cracking in additively-manufactured superalloys, *Acta Mater.* 177 (2019) 209–221, doi:10.1016/j.actamat.2019.07.041.
- [26] J.N. DuPont, J.C. Lippold, S.D. Kiser, *Welding Metallurgy and Weldability of Nickel-Base Alloys*, John Wiley & Sons, Inc., Hoboken, NJ, USA, 2009, doi:10.1002/9780470500262.
- [27] P. Mercelis, J.P. Kruth, Residual stresses in selective laser sintering and selective laser melting, *Rapid Prototyp. J.* 12 (2006) 254–265, doi:10.1108/13552540610707013.

- [28] L.N. Carter, M.M. Attallah, R.C. Reed, Laser powder bed fabrication of nickel-base superalloys: influence of parameters; characterisation, quantification and mitigation of cracking, in: *Superalloys 2012*, John Wiley & Sons, Inc., Hoboken, NJ, USA, 2012, pp. 577–586, doi:10.1002/9781118516430.ch64.
- [29] M.J. Donachie, S.J. Donachie, *Superalloys A Technical Guide*, ASM International, 2002.
- [30] M.D. ROWE, Ranking the resistance of wrought superalloys to strain-age cracking, *Weld. Res.* (2006) 27–34.
- [31] J.F. Barker, The initial years of alloy 718: A GE perspective, in: *Superalloy 719-Metallurgy and Applications*, TMS, 1989, pp. 269–277, doi:10.7449/1989/Superalloys_1989_269_277.
- [32] I.S. Kim, B.G. Choi, H.U. Hong, Y.S. Yoo, C.Y. Jo, Anomalous deformation behavior and twin formation of Ni-base superalloys at the intermediate temperatures, *Mater. Sci. Eng. A* 528 (2011) 7149–7155, doi:10.1016/j.msea.2011.05.083.
- [33] A.A.N. Németh, D.J. Crudden, D.E.J. Armstrong, D.M. Collins, K. Li, A.J. Wilkinson, C.R.M. Grovenor, R.C. Reed, Environmentally-assisted grain boundary attack as a mechanism of embrittlement in a nickel-based superalloy, *Acta Mater.* 126 (2017) 361–371, doi:10.1016/j.actamat.2016.12.039.
- [34] A.J.J.M. G.A. Young, T.E. Capobianco, M.A. Penik, B.W. Morris, The mechanism of ductility dip cracking in Nickel-chromium alloys, *Weld. Res.* (2008).
- [35] D. Qian, J. Xue, A. Zhang, Y. Li, N. Tamura, Z. Song, K. Chen, Statistical study of ductility-dip cracking induced plastic deformation in polycrystalline laser 3D printed Ni-based superalloy, *Sci. Rep.* 7 (2017) 2859, doi:10.1038/s41598-017-03051-x.
- [36] B. Hemsworth, T. Boniszewski, N.F. Eaton, Classification and definition of high temperature welding cracks in alloys, *Met. Constr. Br. Weld. J.* 1 (1969) 5–16.
- [37] L.N. Carter, C. Martin, P.J. Withers, M.M. Attallah, The influence of the laser scan strategy on grain structure and cracking behaviour in SLM powder-bed fabricated nickel superalloy, *J. Alloy. Compd.* 615 (2014) 338–347, doi:10.1016/j.jallcom.2014.06.172.
- [38] A. Ramirez, J. Lippold, High temperature behavior of Ni-base weld metal: part I. Ductility and microstructural characterization, *Mater. Sci. Eng. A* 380 (2004) 259–271, doi:10.1016/j.msea.2004.03.074.
- [39] A. Ramirez, J. Lippold, High temperature behavior of Ni-base weld metal: part II – Insight into the mechanism for ductility dip cracking, *Mater. Sci. Eng. A* 380 (2004) 245–258, doi:10.1016/j.msea.2004.03.075.
- [40] F.F. Noecker, J.N. Dupont, Metallurgical investigation into ductility dip cracking in Ni-based alloys: part II, *Weld. Res.* 88 (2009).
- [41] X.J. Wu, A.K. Koul, Grain boundary sliding in the presence of grain boundary precipitates during transient creep, *Metall. Mater. Trans. A* 26 (1995) 905–914, doi:10.1007/BF02649087.
- [42] Y.T. Tang, A.J. Wilkinson, R.C. Reed, Grain boundary serration in Nickel-based superalloy inconel 600: Generation and effects on mechanical behavior, *Metall. Mater. Trans. A* (2018), doi:10.1007/s11661-018-4671-7.
- [43] J. Xu, H. Gruber, R. Lin Peng, J. Moverare, A novel γ' -strengthened nickel-based superalloy for laser powder bed fusion, *Materials (Basel)* 13 (2020) 4930, doi:10.3390/ma13214930.
- [44] David P. Mourer, Eric S. Huron, Kenneth R. Bain, Enrique E. Montero, Paul L. Reynolds, John J. Schirra, Superalloy optimized for high-temperature performance in high-pressure turbine disks, US 6,521,175 B1, 1998.
- [45] F. Bachmann, R. Hielscher, H. Schaeben, Texture analysis with MTEX – free and open source software toolbox, *Solid State Phenom.* 160 (2010) 63–68, doi:10.4028/www.scientific.net/SSP.160.63.
- [46] K. Thompson, D. Lawrence, D.J. Larson, J.D. Olson, T.F. Kelly, B. Gorman, *In situ* site-specific specimen preparation for atom probe tomography, *Ultramicroscopy* 107 (2007) 131–139, doi:10.1016/j.ultramic.2006.06.008.
- [47] C. Weingarten, D. Buchbinder, N. Pirch, W. Meiners, K. Wissenbach, R. Poprawe, Formation and reduction of hydrogen porosity during selective laser melting of AlSi10Mg, *J. Mater. Process. Technol.* 221 (2015) 112–120, doi:10.1016/j.jmatprotec.2015.02.013.
- [48] A. Hariharan, L. Lu, J. Risse, A. Kostka, B. Gault, E.A. Jägle, D. Raabe, Misorientation-dependent solute enrichment at interfaces and its contribution to defect formation mechanisms during laser additive manufacturing of superalloys, *Phys. Rev. Mater.* 3 (2019) 123602, doi:10.1103/PhysRevMaterials.3.123602.
- [49] Y.T. Tang, C. Panwisawas, J.N. Ghoussoub, Y. Gong, J. Clark, A. Németh, D.G. McCartney, R.C. Reed, Alloys-by-design: application to new superalloys for additive manufacturing, *Acta Mater.* (2020), doi:10.1016/j.actamat.2020.09.023.
- [50] C. Campbell, W. Boettinger, U. Kattner, Development of a diffusion mobility database for Ni-base superalloys, *Acta Mater.* 50 (2002) 775–792, doi:10.1016/S1359-6454(01)00383-4.
- [51] O.M.D.M. Messé, R. Muñoz-Moreno, T. Illston, S. Baker, H.J. Stone, Metastable carbides and their impact on recrystallisation in IN738LC processed by selective laser melting, *Addit. Manuf.* 22 (2018) 394–404, doi:10.1016/j.addma.2018.05.030.
- [52] J. Xu, H. Gruber, R. Boyd, S. Jiang, R.L. Peng, J.J. Moverare, On the strengthening and embrittlement mechanisms of an additively manufactured Nickel-base superalloy, *Materialia* 10 (2020) 100657, doi:10.1016/j.mtla.2020.100657.
- [53] S. Griffiths, H. Ghasemi Tabasi, T. Ivas, X. Maeder, A. De Luca, K. Zwiack, R. Wróbel, J. Jhabvala, R.E. Logé, C. Leinenbach, Combining alloy and process modification for micro-crack mitigation in an additively manufactured Ni-base superalloy, *Addit. Manuf.* 36 (2020) 101443, doi:10.1016/j.addma.2020.101443.
- [54] W.M. Tucho, P. Cuvillier, A. Sjolyst-Kverneland, V. Hansen, Microstructure and hardness studies of Inconel 718 manufactured by selective laser melting before and after solution heat treatment, *Mater. Sci. Eng. A* 689 (2017) 220–232, doi:10.1016/j.msea.2017.02.062.
- [55] A.S. Shaikh, F. Schulz, K. Minet-Lallemand, E. Hryha, Microstructure and mechanical properties of Haynes 282 superalloy produced by laser powder bed fusion, *Mater. Today Commun.* 26 (2021) 102038, doi:10.1016/j.mtcomm.2021.102038.
- [56] X. Wang, L.N. Carter, B. Pang, M.M. Attallah, M.H. Loretto, Microstructure and yield strength of SLM-fabricated CM247LC Ni-Superalloy, *Acta Mater.* 128 (2017) 87–95, doi:10.1016/j.actamat.2017.02.007.
- [57] V.D. Divya, R. Muñoz-Moreno, O.M.D.M. Messé, J.S. Barnard, S. Baker, T. Illston, H.J. Stone, Microstructure of selective laser melted CM247LC nickel-based superalloy and its evolution through heat treatment, *Mater. Charact.* 114 (2016) 62–74, doi:10.1016/j.matchar.2016.02.004.
- [58] N.A. Ahmad, A.A. Wheeler, W.J. Boettinger, G.B. McFadden, Solute trapping and solute drag in a phase-field model of rapid solidification, *Phys. Rev. E* 58 (1998) 3436–3450, doi:10.1103/PhysRevE.58.3436.
- [59] G. Del Guercio, D.G. McCartney, N.T. Aboulkhair, S. Robertson, R. MacLachlan, C. Tuck, M. Simonelli, Cracking behaviour of high-strength AA2024 aluminium alloy produced by laser powder bed fusion, *Addit. Manuf.* 54 (2022) 102776, doi:10.1016/j.addma.2022.102776.
- [60] T. DebRoy, H.L. Wei, J.S. Zuback, T. Mukherjee, J.W. Elmer, J.O. Milewski, A.M. Beese, A. Wilson-Heid, A. De, W. Zhang, Additive manufacturing of metallic components – Process, structure and properties, *Prog. Mater. Sci.* 92 (2018) 112–224, doi:10.1016/j.pmatsci.2017.10.001.
- [61] A.J. Elliott, T.M. Pollock, S. Tin, W.T. King, S.C. Huang, M.F.X. Gigliotti, Directional solidification of large superalloy castings with radiation and liquid-metal cooling: A comparative assessment, *Metall. Mater. Trans. A* 35 (2004) 3221–3231, doi:10.1007/s11661-004-0066-z.
- [62] J. Xu, Alloy Design and Characterization of γ' Strengthened Nickel-based Superalloys for Additive Manufacturing, Linköping University Electronic Press, 2021, doi:10.3384/lic.diva-173042.
- [63] G. Abreu Faria, K. Kadirvel, A. Hinojos, W. Zhang, Y. Wang, A.J. Ramirez, On the use of metastable interface equilibrium assumptions on prediction of solidification micro-segregation in laser powder bed fusion, *Sci. Technol. Weld. Join.* 24 (2019) 446–456, doi:10.1080/13621718.2019.1608406.
- [64] A. Després, S. Antonov, C. Mayer, C. Tassin, M. Veron, J.J. Blandin, P. Kontis, G. Martin, On the role of boron, carbon and zirconium on hot cracking and creep resistance of an additively manufactured polycrystalline superalloy, *Materialia* 19 (2021) 101193, doi:10.1016/j.mtla.2021.101193.
- [65] J.H. Boswell, D. Clark, W. Li, M.M. Attallah, Cracking during thermal post-processing of laser powder bed fabricated CM247LC Ni-superalloy, *Mater. Des.* 174 (2019) 107793, doi:10.1016/j.matdes.2019.107793.
- [66] N. Zhou, A.D. Dicus, S.A.J. Forsik, T. Wang, G.A. Colombo, M.E. Epler, Development of a new alumina-forming crack-resistant high- γ' fraction Ni-base Superalloy for additive manufacturing, in: *Superalloys 2020*, TMS, 2020, pp. 1046–1054, doi:10.1007/978-3-030-51834-9_102.
- [67] L.N. Carter, X. Wang, N. Read, R. Khan, M. Aristizabal, K. Essa, M.M. Attallah, Process optimisation of selective laser melting using energy density model for nickel based superalloys, *Mater. Sci. Technol.* 32 (2016) 1–5, doi:10.1179/1743284715Y.0000000108.
- [68] N. Kalentics, N. Sohrabi, H.G. Tabasi, S. Griffiths, J. Jhabvala, C. Leinenbach, A. Burn, R.E. Logé, Healing cracks in selective laser melting by 3D laser shock peening, *Addit. Manuf.* 30 (2019) 100881, doi:10.1016/j.addma.2019.100881.
- [69] S. Catchpole-Smith, N. Aboulkhair, L. Parry, C. Tuck, I.A.A. Ashcroft, A. Clare, Fractal scan strategies for selective laser melting of 'unweldable' nickel superalloys, *Addit. Manuf.* 15 (2017) 113–122, doi:10.1016/j.addma.2017.02.002.
- [70] S. Pourbabak, M.L. Montero-Sistiaga, D. Schryvers, J. Van Humbeeck, K. Vanmeensel, Microscopic investigation of as built and hot isostatic pressed Hastelloy X processed by Selective Laser Melting, *Mater. Charact.* 153 (2019) 366–371, doi:10.1016/j.matchar.2019.05.024.
- [71] O. Sanchez-Mata, X. Wang, J. Muñiz-Lerma, M. Attarian Shandiz, R. Gauvin, M. Brochu, Fabrication of crack-free nickel-based superalloy considered non-weldable during laser powder bed fusion, *Materials (Basel)* 11 (2018) 1288, doi:10.3390/ma11081288.
- [72] A. Iveković, M.L. Montero-Sistiaga, J. Vleugels, J.P. Kruth, K. Vanmeensel, Crack mitigation in Laser powder bed fusion processed hastelloy X using a combined numerical-experimental approach, *J. Alloy. Compd.* 864 (2021) 158803, doi:10.1016/j.jallcom.2021.158803.
- [73] Christofidou, K.A. et al. (2020). Microstructural Control and Optimization of Haynes 282 Manufactured Through Laser Powder Bed Fusion. In: , et al. *Superalloys 2020*. The Minerals, Metals & Materials Series. Springer, Cham. doi:10.1007/978-3-030-51834-9_99.
- [74] C. Qiu, H. Chen, Q. Liu, S. Yue, H. Wang, On the solidification behaviour and cracking origin of a nickel-based superalloy during selective laser melting, *Mater. Charact.* 148 (2019) 330–344, doi:10.1016/j.matchar.2018.12.032.
- [75] R. Engeli, T. Etter, S. Hövel, K. Wegener, Processability of different IN738LC powder batches by selective laser melting, *J. Mater. Process. Technol.* 229 (2016) 484–491, doi:10.1016/j.jmatprotec.2015.09.046.
- [76] Y. HU, X. YANG, W. KANG, Y. DING, J. XU, H. ZHANG, Effect of Zr content on crack formation and mechanical properties of IN738LC processed by selective laser melting, *Trans. Nonferr. Met. Soc. China* 31 (2021) 1350–1362, doi:10.1016/S1003-6326(21)65582-6.
- [77] M. Cloots, K. Kunze, P.J. Uggowitzer, K. Wegener, Microstructural characteristics of the nickel-based alloy IN738LC and the cobalt-based alloy Mar-M509

- produced by selective laser melting, *Mater. Sci. Eng. A* 658 (2016) 68–76, doi:10.1016/j.msea.2016.01.058.
- [78] N. Perevoshchikova, J. Rigaud, Y. Sha, M. Heilmaier, B. Finnin, E. Labelle, X. Wu, Optimisation of selective laser melting parameters for the Ni-based superalloy IN-738 LC using Doehlert's design, *Rapid Prototyp. J.* 23 (2017) 881–892, doi:10.1108/RPJ-04-2016-0063.
- [79] M. Cloots, P.J. Uggowitzer, K. Wegener, Investigations on the microstructure and crack formation of IN738LC samples processed by selective laser melting using Gaussian and doughnut profiles, *Mater. Des.* 89 (2016) 770–784, doi:10.1016/j.matdes.2015.10.027.
- [80] A. De Luca, C. Kenel, S. Griffiths, S.S. Joglekar, C. Leinenbach, D.C. Dunand, Microstructure and defects in a Ni-Cr-Al-Ti γ/γ' model superalloy processed by laser powder bed fusion, *Mater. Des.* 201 (2021), doi:10.1016/j.matdes.2021.109531.
- [81] T. Vilaro, C. Colin, J.D. Bartout, L. Nazé, M. Sennour, Microstructural and mechanical approaches of the selective laser melting process applied to a nickel-base superalloy, *Mater. Sci. Eng. A* 534 (2012) 446–451, doi:10.1016/j.msea.2011.11.092.
- [82] E.I. Galindo-Nava, L.D. Connor, C.M.F. Rae, On the prediction of the yield stress of unimodal and multimodal γ/γ' Nickel-base superalloys, *Acta Mater.* 98 (2015) 377–390, doi:10.1016/j.actamat.2015.07.048.
- [83] R.D.D. Bert Verlinden, J. Driver, I. Samajdar, Chapter 4 Work hardening, in: *Thermo-Mechanical Processing of Metallic Materials*, Elsevier, 2007, pp. 55–81, doi:10.1016/S1470-1804(07)80008-3.
- [84] Y.K. Kim, J. Choe, K.A. Lee, Selective laser melted equiatomic CoCrFeMnNi high-entropy alloy: Microstructure, anisotropic mechanical response, and multiple strengthening mechanism, *J. Alloy. Compd.* 805 (2019) 680–691, doi:10.1016/j.jallcom.2019.07.106.
- [85] K.M. Bertsch, G. Meric de Bellefon, B. Kuehl, D.J. Thoma, Origin of dislocation structures in an additively manufactured austenitic stainless steel 316L, *Acta Mater.* 199 (2020) 19–33, doi:10.1016/j.actamat.2020.07.063.
- [86] A.W. Thompson, Substructure strengthening mechanisms, *Metall. Trans. A* 8 (1977) 833–842, doi:10.1007/BF02661564.
- [87] U.F. Kocks, H. Mecking, Physics and phenomenology of strain hardening: the FCC case, *Prog. Mater. Sci.* 48 (2003) 171–273, doi:10.1016/S0079-6425(02)00003-8.
- [88] G. Marchese, M. Lorusso, S. Parizia, E. Bassini, J.W. Lee, F. Calignano, D. Manfredi, M. Turner, H.U. Hong, D. Uguets, M. Lombardi, S. Biamino, Influence of heat treatments on microstructure evolution and mechanical properties of Inconel 625 processed by laser powder bed fusion, *Mater. Sci. Eng. A* 729 (2018) 64–75, doi:10.1016/j.msea.2018.05.044.
- [89] Q. Han, Y. Gu, R. Setchi, F. Lacan, R. Johnston, S.L. Evans, S. Yang, Additive manufacturing of high-strength crack-free Ni-based Hastelloy X superalloy, *Addit. Manuf.* 30 (2019) 100919, doi:10.1016/j.addma.2019.100919.
- [90] C.H. Yu, R.L. Peng, M. Calmunge, V. Luzin, H. Brodin, J. Moverare, *Anisotropic Deformation and Fracture Mechanisms of an Additively Manufactured Ni-Based Superalloy*, Springer, Cham, 2020, pp. 1003–1013.
- [91] P. Kanagarajah, F. Brenne, T. Niendorf, H.J.J. Maier, Inconel 939 processed by selective laser melting: effect of microstructure and temperature on the mechanical properties under static and cyclic loading, *Mater. Sci. Eng. A* 588 (2013) 188–195, doi:10.1016/j.msea.2013.09.025.
- [92] H.A. Roth, C.L. Davis, R.C. Thomson, Modeling solid solution strengthening in nickel alloys, *Metall. Mater. Trans. A* 28 (1997) 1329–1335, doi:10.1007/s11661-997-0268-2.
- [93] B. Gan, S. Tin, Assessment of the effectiveness of transition metal solutes in hardening of Ni solid solutions, *Mater. Sci. Eng. A* 527 (2010) 6809–6815, doi:10.1016/j.msea.2010.06.071.
- [94] M. Sadowski, L. Ladani, W. Brindley, J. Romano, Optimizing quality of additively manufactured Inconel 718 using powder bed laser melting process, *Addit. Manuf.* 11 (2016) 60–70, doi:10.1016/j.addma.2016.03.006.
- [95] H. Wang, X. Zhang, G.B. Wang, J. Shen, G.Q. Zhang, Y.P. Li, M. Yan, Selective laser melting of the hard-to-weld IN738LC superalloy: efforts to mitigate defects and the resultant microstructural and mechanical properties, *J. Alloy. Compd.* 807 (2019) 151662, doi:10.1016/j.jallcom.2019.151662.
- [96] J. Yang, F. Li, A. Pan, H. Yang, C. Zhao, W. Huang, Z. Wang, X. Zeng, X. Zhang, Microstructure and grain growth direction of SRR99 single-crystal superalloy by selective laser melting, *J. Alloy. Compd.* 808 (2019) 151740, doi:10.1016/j.jallcom.2019.151740.
- [97] Z. Chen, S. Chen, Z. Wei, L. Zhang, P. Wei, B. Lu, S. Zhang, Y. Xiang, Anisotropy of nickel-based superalloy K418 fabricated by selective laser melting, *Prog. Nat. Sci. Mater. Int.* 28 (2018) 496–504, doi:10.1016/j.pnsc.2018.07.001.
- [98] G. Marchese, S. Parizia, M. Rashidi, A. Saboori, D. Manfredi, D. Uguets, M. Lombardi, E. Hryha, S. Biamino, The role of texturing and microstructure evolution on the tensile behavior of heat-treated Inconel 625 produced via laser powder bed fusion, *Mater. Sci. Eng. A* 769 (2020) 138500, doi:10.1016/j.msea.2019.138500.
- [99] D. Zhang, W. Niu, X. Cao, Z. Liu, Effect of standard heat treatment on the microstructure and mechanical properties of selective laser melting manufactured Inconel 718 superalloy, *Mater. Sci. Eng. A* 644 (2015) 32–40, doi:10.1016/j.msea.2015.06.021.
- [100] Y.L. Kuo, S. Horikawa, K. Kakehi, Effects of build direction and heat treatment on creep properties of Ni-base superalloy built up by additive manufacturing, *Scr. Mater.* 129 (2017) 74–78, doi:10.1016/j.scriptamat.2016.10.035.
- [101] Roman ENGELI, Thomas Etter, Hossein Meidani, Gamma prime precipitation strengthened nickel-base superalloy for use in powder based additive manufacturing process, US 2017/0021453 A1, 2016.
- [102] G. Marchese, S. Parizia, A. Saboori, D. Manfredi, M. Lombardi, P. Fino, D. Uguets, S. Biamino, The influence of the process parameters on the densification and microstructure development of laser powder bed fused inconel 939, *Metals (Basel)* 10 (2020) 882, doi:10.3390/met10070882.
- [103] Y. Hagedorn, J. Risse, W. Meiners, N. Pirch, K. Wissenbach, R. Poprawe, Processing of nickel based superalloy MAR M-247 by means of High Temperature – Selective Laser Melting (HT – SLM), in: *High Value Manufacturing: Advanced Research in Virtual and Rapid Prototyping*, CRC Press, 2013, pp. 291–295, doi:10.1201/b15961-54.
- [104] I. Lopez-Galilea, B. Ruttert, J. He, T. Hammerschmidt, R. Drautz, B. Gault, W. Theisen, Additive manufacturing of CMSX-4 Ni-base superalloy by selective laser melting: influence of processing parameters and heat treatment, *Addit. Manuf.* 30 (2019) 100874, doi:10.1016/j.addma.2019.100874.
- [105] K. Peng, R. Duan, Z. Liu, X. Lv, Q. Li, F. Zhao, B. Wei, B. Nong, S. Wei, Cracking behavior of René 104 Nickel-based superalloy prepared by selective laser melting using different scanning strategies, *Materials (Basel)* 13 (2020) 2149, doi:10.3390/ma13092149.
- [106] B. Wei, Z. Liu, B. Nong, B. Cao, X. Lv, Y. Ren, Y. Ai, Microstructure, cracking behavior and mechanical properties of René 104 superalloy fabricated by selective laser melting, *J. Alloy. Compd.* 867 (2021) 158377, doi:10.1016/j.jallcom.2020.158377.
- [107] B. Wei, Z. Liu, B. Cao, B. Nong, Y. Zhang, Y. Ren, H. Zhou, S. Wei, Cracking inhibition of nano-TiC reinforced René 104 superalloy fabricated by selective laser melting, *J. Alloy. Compd.* (2021) 160413, doi:10.1016/j.jallcom.2021.160413.
- [108] S.P. Murray, K.M. Pusch, A.T. Polonsky, C.J. Torbet, G.G.E.E. Seward, N. Zhou, S.A.J.J. Forsik, P. Nandwana, M.M. Kirka, R.R. Dehoff, W.E. Slye, T.M. Pollock, A defect-resistant Co–Ni superalloy for 3D printing, *Nat. Commun.* 11 (2020) 4975, doi:10.1038/s41467-020-18775-0.
- [109] A. Chakraborty, R. Tangestani, W. Muhammad, T. Sabiston, J.P. Masse, R. Batmaz, A. Wessman, É. Martin, Micro-cracking mechanism of RENÉ 108 thin-wall components built by laser powder bed fusion additive manufacturing, *Mater. Today Commun.* 30 (2022) 103139, doi:10.1016/j.mtcomm.2022.103139.
- [110] S.A. Götelid Sareh, Ma Taoran, L. Christophe, V. Jesper, S. Emil, H. Jonas, H. Seyed, Effect of post-processing on microstructure and mechanical properties of Alloy 718 fabricated using powder bed fusion additive manufacturing processes, *Rapid Prototyp. J.* (2021), doi:10.1108/RPJ-12-2019-0310.
- [111] Z. Chen, Y. Lu, F. Luo, S. Zhang, P. Wei, S. Yao, Y. Wang, Effect of laser scanning speed on the microstructure and mechanical properties of laser-powder-bed-fused K418 Nickel-based alloy, *Materials (Basel)* 15 (2022) 3045, doi:10.3390/ma15093045.
- [112] S.E. Atabay, O. Sanchez-Mata, J.A. Muñoz-Lerma, M. Brochu, Microstructure and mechanical properties of difficult to weld Rene 77 superalloy produced by laser powder bed fusion, *Mater. Sci. Eng. A* 827 (2021) 142053, doi:10.1016/j.msea.2021.142053.
- [113] S.E. Atabay, O. Sanchez-Mata, J.A. Muñoz-Lerma, R. Gauvin, M. Brochu, Microstructure and mechanical properties of rene 41 alloy manufactured by laser powder bed fusion, *Mater. Sci. Eng. A* 773 (2020) 138849, doi:10.1016/j.msea.2019.138849.
- [114] C.S.S.M. Prager, *Welding of precipitation-hardening Nickel-base alloys*, *Weld. Res. Coun. Bull.* (1968) 1–55.